Sister Rod Destructive Examinations (FY21)

Appendix B: Segmentation, Defueling, Metallographic Data and Total Cladding Hydrogen

Spent Fuel and Waste Disposition

Prepared for
US Department of Energy

Spent Fuel and Waste Science and Technology

Oak Ridge National Laboratory

Rose Montgomery, Tyson Jordan, James T. Dixon, Stephanie M. Curlin, Jason Harp

March 31, 2022

M2SF-22OR010201042

ORNL/SPR-2021/2279

ORNL/SPR-2020/1744 revision 1

SUMMARY

This report documents work performed under the Spent Fuel and Waste Disposition's Spent Fuel and Waste Science and Technology program for the US Department of Energy (DOE) Office of Nuclear Energy (NE). This work was performed to fulfill Level 2 Milestone M2SF-22OR010201042, "FY2021 ORNL Report on High Burnup Sibling Pin Testing Results," within work package SF-22OR01020104 and is an update to the work reported in M2SF-21OR010201032, M2SF-19ORO010201026 and M2SF-19OR010201028.

As a part of the DOE-NE High Burnup Spent Fuel Data Project, Oak Ridge National Laboratory (ORNL) is performing destructive examinations (DEs) of high burnup (HBU) (>45 GWd/MTU) spent nuclear fuel (SNF) rods from the North Anna Nuclear Power Station operated by Dominion Energy. The SNF rods, called *sister rods* or *sibling rods* are all HBU and include four different kinds of fuel rod cladding: standard Zircaloy-4 (Zirc-4), low-tin (LT) Zirc-4, ZIRLO®, and M5®. The DEs are being conducted to obtain a baseline of the HBU rod's condition before dry storage and are focused on understanding overall SNF rod strength and durability. Both composite fuel and defueled cladding will be tested to derive material properties. Although the data generated can be used for multiple purposes, one primary goal for obtaining the post-irradiation examination data and associated measured mechanical properties is to support SNF dry storage licensing and relicensing activities by (1) addressing identified knowledge gaps and (2) enhancing the technical basis for post-storage transportation, handling, and subsequent disposition of the SNF.

This report documents the status of the ORNL Phase 1 DE activities related to:

- Rough segmentation (RS),
- Defueling (DEF)
- DE.02 optical microscopy (MET)
- DE.03, cladding total hydrogen measurements

for seven Phase 1 sister rods. This report also outlines the DE tasks performed and the data collected to date, as guided by the sister rod test plans.

Appendix B provides detailed information regarding defueling activities, metallographic imaging and measurements, and total cladding hydrogen measurements.

Table SB-1 provides the status of the DE activities discussed in this appendix.

Table SB-1. DE status.

Planned DE		Status	ORNL lead	Comments
RS	Rough segmentation	Complete	Morris / Burns	All rough segmentation is complete for Phase 1 rods
DEF	Defueling	In progress	Montgomery	The majority of the defueling is complete. Additional defueling of DE.02 and DE.03 specimens is being performed as needed.
DE.02	Optical microscopy (MET)	In progress	Jordan (fueled); Dixon / Curlin (defueled)	Fueled and defueled specimens are being prepared for MET views. The Phase 1 priority 1 specimens were cut, and specimen preparation/polishing is in progress. Cladding/pellet views and measurements are available for all Phase 1 rods. Specific features, including waterside oxide thickness, remaining cladding wall thickness, pellet-side oxide thickness, HBU rim, and cladding inner and outer diameters were measured. Where applicable, comparisons with nondestructive examinations were provided. Section views were inspected for hydride orientation, and radial hydrides are visible in the heat-treated M5-clad specimen and the ZIRLO-clad heat-treated specimen. There is a high hydride density in the heat-treated Zirc-4 specimen. The few radial hydrides are short. The baseline ZIRLO-clad specimen includes short radial hydrides. The other baseline specimens did not have radial hydrides. An axial MET was created at a pellet-pellet gap. Axial and radial METs do not show a change in the hydride precipitation density through the gap. A section of the cladding will be analyzed for total hydrogen content to determine whether the total cladding hydrogen content varies between the pelleted region and the pellet-pellet gap. Other rod elevations are slated for MET views, and the work will continue.
DE.03	Cladding total hydrogen measurements	Measurements in progress	Harp	Specimens were defueled and the equipment was set up. Out-of-cell verification testing of the oxygen nitrogen hydrogen analyzer is complete, and it has been installed in the Irradiated Fuels Examination Laboratory (IFEL) greenhouse in a separate enclosure. Of the 20 planned measurements, 14 have been completed to date.

ACKNOWLEDGMENTS

Many thanks to our US Department of Energy Office of Nuclear Energy sponsor Ned Larson, along with the Spent Fuel and Waste Science and Technology (SFWST) storage and transportation program leadership for their continued support. The sister rod project would not be possible without the vision and support of the Electric Power Research Institute, Westinghouse, Framatome, and Dominion Energy.

This work would not be possible without the support and expertise provided by the leadership and staff members of the Oak Ridge National Laboratory (ORNL) Irradiated Fuel Examination Laboratory (IFEL). Special thanks go to John Hinds and Brian Woody, the Building 3525 operators; and to Tracy Binger and Mark Walls for their assistance with the defueling, cleaning, and irradiated material handling. Rick Henry has the unenviable task of tracking the bits and pieces of sister rods and their moves around the hot cell and to other facilities, and we very much appreciate his patience and continued support.

Special thanks go to Tyler Smith for his work developing a defueling column for the sister rod fuel material. We appreciate his continuing support, along with the ongoing efforts from Lindsey Aloisi, to defuel the many small specimens required for total cladding hydrogen and metallographic studies. We also appreciate Tracy Binger's efforts measuring and tracking the defueled cladding radiation levels in support of releasing the specimens to ORNL's Low Activation Materials Development and Analysis (LAMDA) lab. Our appreciation and thanks are extended to Josh Schmidlin, Thomas Muth, and the LAMDA lab staff for their continuing support on the sister rod metallography. For their wise advice and support deploying new equipment and processes at IFEL, we appreciate Jim Miller and Mark Delph.

This page is intentionally left blank.

CONTENTS

This page is intentionally left blank.

LIST OF FIGURES

LIST OF TABLES

This page is intentionally left blank.

REVISION HISTORY

Date	Changes
3/29/2019	Initial release
9/27/2019	Revised to include additional data and incorporate comments from the previously released report.
10/30/2020	Initial release of this appendix.
11/30/2020	The document numbering was revised to reflect its 2020 M2 status and the date was changed.
10/29/2021	Section B-4 was added.
3/31/2022	Comments received on the 10/29/2021 manuscript were incorporated throughout. The document numbering was revised to reflect its 2021 M2 status and the date was changed.

This page is intentionally left blank.

ACRONYMS

CIRFT	Cyclic Integral Reversible Fatigue Tester
DE	destructive examination
DEF	defueling
DOE	US Department of Energy
EPRI	Electric Power Research Institute
FHT	full-length fuel rod heat treatment
FY	fiscal year
GTRF	grid-to-rod fretting
HBU	high burnup
HPU	hydrogen pickup
ID	inner diameter
IFEL	Irradiated Fuels Examination Laboratory
LAMDA	Low Activation Materials Development and Analysis
LT	low tin
LVDT	linear variable differential transducer
MET	metallography
NE	Office of Nuclear Energy
NDE	nondestructive examination
OD	outer diameter
ONH	oxygen nitrogen hydrogen
ORNL	Oak Ridge National Laboratory
PWR	pressurized water reactor
RPC	Research Project Cask
RS	rough segmentation
SFWST	Spent Fuel and Waste Science and Technology
SEM	scanning electron microscope
SNF	spent nuclear fuel
TEM	transmission electron microscope

This page is intentionally left blank

B-1. ROUGH SEGMENTATION (RS)

Seven Phase 1 rods [B-1,B-2,B-3] were segmented:

- 30AD05 (M5 clad)
- 30AE14 (M5 clad, heat-treated)
- 3D8E14 (ZIRLO clad)
- 3F9N05 (ZIRLO clad, heat-treated)
- F35P17 (Zirc-4 clad, heat-treated)
- 3A1F05 (LT Zirc-4 clad)
- 6U3K09 (ZIRLO clad)

A detailed cutting plan was developed [B-3], with test specimens allocated for the destructive examinations (DEs) as guided by the test plans [B-2,B-3] and the results of the nondestructive examination (NDE) [B-4]. Each segment was marked to indicate the upper elevation and placed into a labeled storage capsule as it was cut. The capsules are not backfilled with inert gas because these Phase 1 rod segments are expected to be used in testing within a few years. The rough segments are further subdivided as needed for the slated DE.

This page is intentionally left blank.

B-2. DEFUELING (DEF)

Many segments will be defueled in the process of specimen preparation for DE. For example, all DE.03 specimens must be defueled before testing. DE.10 includes fueled and defueled specimens. In some cases, the removed fuel is the target of the test (e.g., DE.01 includes burnup measurements). The defueling processes vary depending on the follow-on tests to be performed. This section briefly describes defueling activities.

B-2.1 Defueling Cladding Segments for Argonne National Laboratory Shipment

Twelve rod cladding segments were selected from the Phase 1 sister rods for ring compression testing as listed in Table B-1. The segments were defueled by boiling them individually in an acid bath, and each piece of defueled cladding was weighed and packaged individually in an aluminum container. The dose rate was measured at contact and at 1 ft. The dose rates represent the hottest spots on the container. The exterior surfaces of the aluminum containers were decontaminated before they were loaded into the shipping container. The dose rate of a decontaminated empty aluminum container is expected to be <20mR/hr. Figure B-1 shows the cladding segments in their aluminum containers awaiting shipment to Argonne National Laboratory and a dose rate measurement being taken on one sample in its aluminum container using a Ludlum 9-4 ion chamber.

To determine the isotopic inventory of any pellet materials that might still be adhered to the interior wall of the cladding following this defueling process, one 18 mm rod segment was defueled using the same process, and then the resulting defueled cladding segment was dissolved and analyzed. The results of the analysis, tabulated in Table B-2, were used to determine the residual pellet material isotopic content of each cladding segment based on the segment's weight.

Shipment of the segments was completed in April 2019.

Table B-1. Defueled cladding specimens for shipment to Argonne National Laboratory

Sister rod and elevation of segment	Aluminum canister weight (g)	Canister + clad weight (g)	Clad weight (g)	Gamma dose on contact (mR/h)	Gamma dose @ 30cm (mR/h)
30AD05-2429-2519-DE.10	10.18	19.20	9.02	1,800	70
30AD05-3259-3349-DE.10	9.97	19.04	9.07	1,800	70
30AE14-2694-2784-DE.10	10.19	19.55	9.36	2,300	100
30AE14-3309-3399-DE.10	10.39	19.76	9.37	1,800	70
3A1F05-2555-2645-DE.10	10.22	19.74	9.52	1,200	50
3A1F05-3015-3105-DE.10	10.41	19.79	9.38	1,000	40
3D8E14-2213-2303-DE.10	10.17	19.68	9.51	1,400	60
3D8E14-2565-2655-DE.10	10.16	19.74	9.58	1,400	60
3F9N05-2572-2662-DE.10	10.22	19.78	9.56	1,400	70
3F9N05-3241-3331-DE.10	10.02	19.60	9.58	1,200	50
F35P17-2555-2645-DE.10	10.16	19.42	9.26	1,200	40
F35P17-3069-3159-DE.10	10.14	19.91	9.77	1,000	40

Table B-2. Residual pellet materials after defueling on an activity per gram of cladding basis

Isotope	Ci/g	Isotope	Ci/g	Isotope	Ci/g
^{60}Co	7.20E-06	^{237}Np	2.14E-10	^{242}Pu	4.81E-09
^{95}Zr	4.15E-06	^{234}U	3.70E-10	^{241}Am	2.85E-06
^{106}Ru	2.08E-05	^{235}U	3.87E-12	^{242m}Am	2.44E-08
^{125}Sb	1.27E-05	^{236}U	1.07E-10	^{243}Am	6.47E-08
^{134}Cs	1.58E-04	^{238}U	7.19E-11	^{244}Cm	1.04E-05
^{137}Cs	1.27E-03	^{238}Pu	3.53E-06	^{245}Cm	2.41E-09
^{144}Ce	4.15E-06	^{239}Pu	3.75E-07	^{246}Cm	9.61E-10
^{154}Eu	5.53E-05	^{240}Pu	5.33E-07	Beta *	3.708E-03
^{155}Eu	1.94E-05	^{241}Pu	0.000147		

* "Beta" is the remaining beta activity after subtracting known beta emitters and G-Alpha results from the liquid scintillation result. It is assumed to represent ^{90}Sr/^{90}Y.

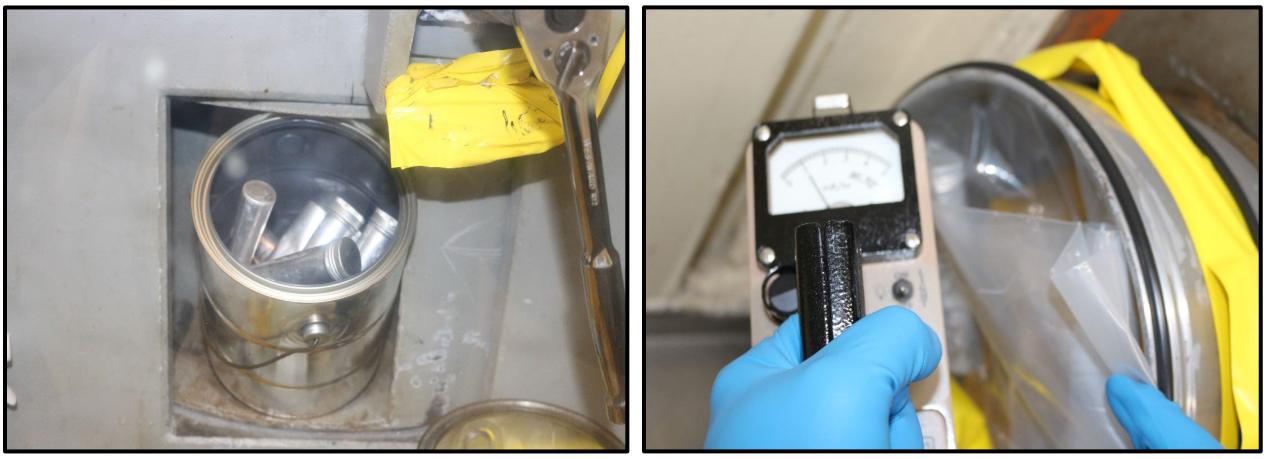

Figure B-1. Defueled cladding segments in aluminum containers awaiting shipment to Argonne (left) and contact dose rate measurement on a single container (right).

B-2.2 Defueling Cladding Segments to Prepare Total Cladding Hydrogen and Metallographic Specimens

To prepare specimens for total cladding hydrogen measurements (DE.03), the fuel is removed from the cladding. Also, it is desired to produce some cladding-only metallographic (DE.02) specimens. To remove the fuel from the cladding for these examinations, a dissolution column was constructed and installed in the IFEL hot cell in March 2019. The column, shown in Figure B-2, incorporates a recirculating acid loop to reduce the volume of waste generated and reduce acid vapor released to the hot cell atmosphere. The design also includes a Soxhlet extractor that periodically flushes the dissolution acid bath from the chamber in which the cladding is held. This provides a supply of clean acid to remove as much fuel as possible. Figure B-2(a) shows a defueled specimen planned for metallographic imaging, and Figure B-2(b) shows the dissolution column in the ORNL hot cell. To date, 13 specimens have been defueled using the dissolution column.

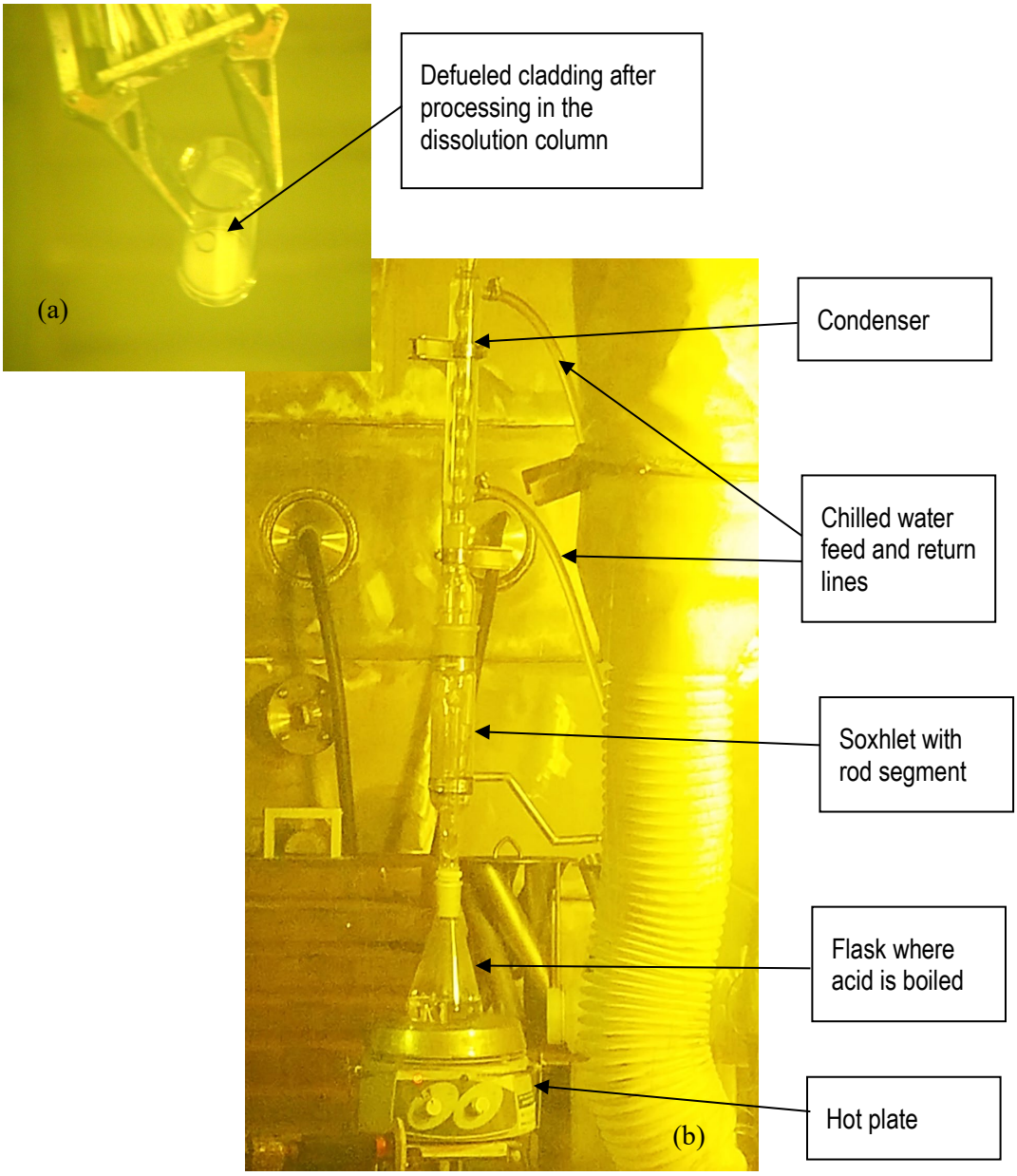

Figure B-2. (a) A Defueled specimen ready for DE.02 or DE.03 after several passes in (b) the dissolution column installed in the ORNL IFEL hot cell.

This page is intentionally left blank.

B-3. METALLOGRAPHY (DE.02)

The rough-cut DE.02 segments provide source material for several exams, including metallographic mounts (METs), total cladding hydrogen analysis, microhardness, scanning electron microscope (SEM), and transmission electron microscope (TEM) imaging. The first step in the DE.02 process is to cut appropriate specimens from the segments for each exam. Approximately ⅓ of the Phase 1 DE-02 segments were sub-sectioned.

For METs, defueled and fueled views were prepared. The fueled views allow pellet features such as cracks and the high burnup (HBU) rim to be inspected, whereas the defueled views typically provide much cleaner, clearer views of the cladding with its hydrides and oxide layers. Figure B-3 provides examples of the typical features discussed within the METs. Not all features are visible in all views. For example, pellet cracks are only visible in fueled full-section METs, as shown in the upper right of Figure B-3. If a feature in the image is straight, then it is likely a polishing artifact or scratch. The waterside and pellet-side can usually be identified by the curvature of the cladding when the pellet is not present. The waterside oxide usually appears flat in cross-sectional METs, and the pellet-side oxide appears wavy in areas where the oxide has grown into the pellet. Cladding hydride precipitates are either dark lines (when defueled and etched) or white lines (in the fueled METs) and either follow the curvature of the cladding or are perpendicular to it. In fueled MET views, pellet porosity is visible as dark spots in the pellet region. For clarity, these typical features are not labeled in every MET and only atypical features are labeled where necessary.

Table B-3 summarizes the Phase 1 DE.02 segments and selected metallographic views, selected specimens for total cladding hydrogen measurements, and the current status of the exams.

METs are available for all seven of the Phase 1 sister rods, but not all planned elevation views are available. Selected representative MET views are organized by cladding type in Sections B-3.1 through B-3.4. A summary of cladding thickness, waterside oxide thickness, pellet-side oxide thickness, and HBU rim measurements taken using the MET views is provided in Table B-4 by rod and elevation where available. The uncertainty of the microscopy measurements is related to the pixel resolution and to the ability of the analyst to visually select the points for measurement. For these measurements the uncertainty is estimated as ±3 μm. As noted in Table B-4, the data for each rod is taken from different elevations from the rod and the use of burnup as a correlating parameter removes the expected differences in rod performance related to specimen elevation on the fuel rod. Most of the measured performance parameters are expected to vary azimuthally within the specimen (except for rod ID and OD) and the number of observations underlying the mean presented in Table B-4 range from 3 to 55 observations. For brevity, not all of the MET views and measurements are provided in this report and, although measurements are shown on some views, not all measurements taken are provided in the MET images selected for inclusion herein.

The minimum remaining wall thickness measured using microscopy is 495 μm for 3A1F05, and the thickest waterside oxide thickness was 128 μm for the same rod, which also had extensive oxide spalling. While the microscopy measurements are considered more accurate than the previously reported nondestructive measurements [B-4], a comparison of the two provides an independent check of the data and the NDE method uncertainty. Table B-5 provides a comparison of the NDE measurements and microscopy measurements. The rod outer diameter (OD) was measured nondestructively using linear variable differential transducers (LVDTs), and the waterside oxide thickness and minimum remaining cladding wall thickness measurements were obtained using eddy current methods [B-4].The LVDT-reported OD seems to be biased on the high side by ~0.5%. The eddy current measurements of remaining wall thickness seem to be biased ~4% on the high side, except for the Zirc-4 and LT-Zirc 4-clad rods. For those cladding alloys, eddy current–measured wall thickness was lower than that measured using the METs. The eddy current–estimated remaining wall thickness for 3A1F05-2735-2754 is ~10% lower than

that measured using the METs. As discussed in the NDE report [B-4], the waterside oxide thickness varies around the circumference of the cladding. Generally, the maximum recorded MET measurements are comparable with the local average eddy current oxide thickness measurements, except for the M5-clad rods, which had oxide thickness in the lower ranges of detectability for the eddy current system used.

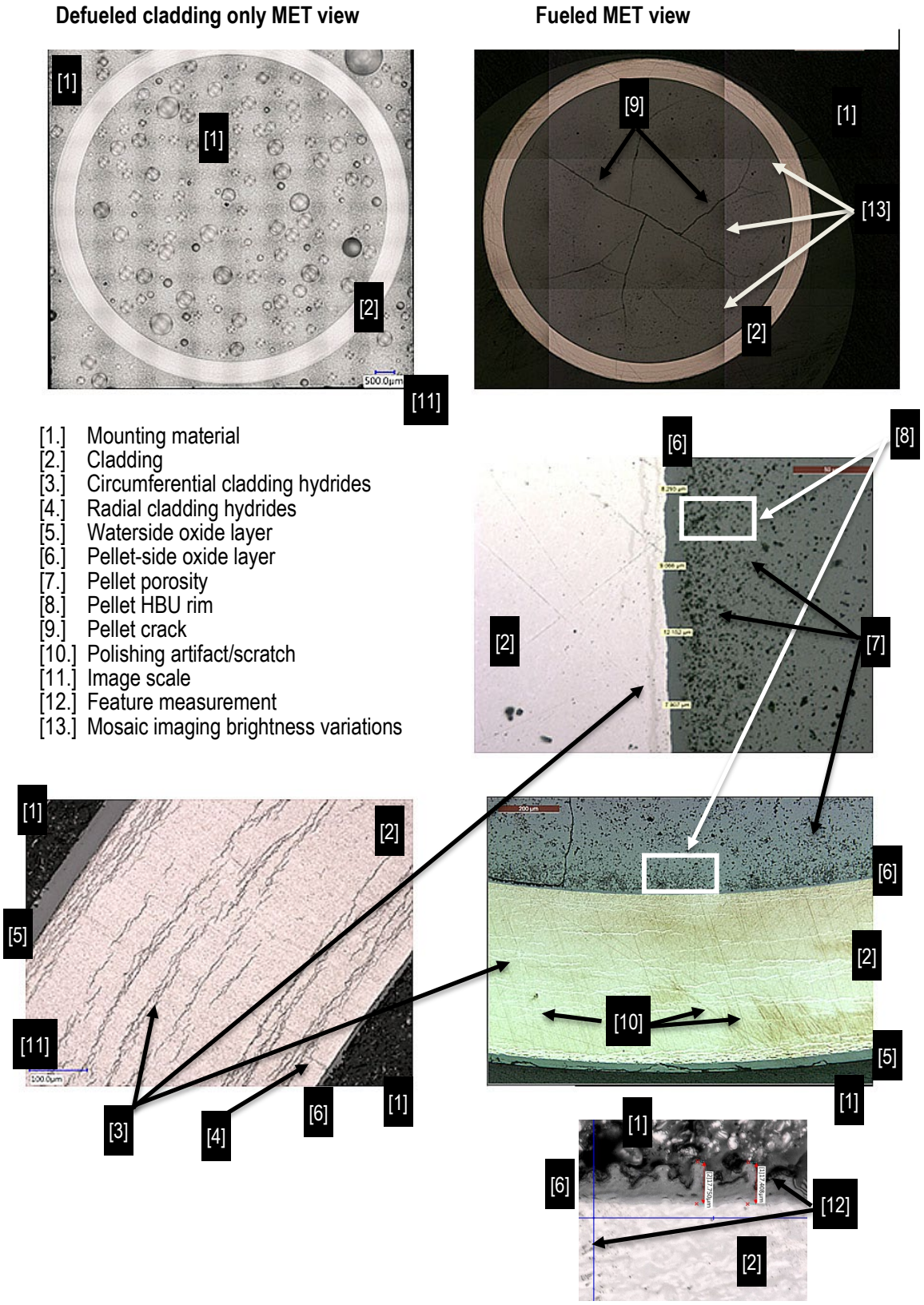

Figure B-3. Example of typical MET views and section features.

Table B-3. Phase 1 DE.02 parent segments with metallographic and total cladding hydrogen specimen selections and status.

Rod and originating segment elevation range (mm)			Fueled or defueled MET	Selection criteria	MET	Total cladding H_2
30AD05	678	697	TBD	Oxide thickness	✓	
30AD05	1,280	1,299	Fueled	Oxide thickness	Mounted	✓
30AD05	2,410	2,429	Defueled	HBU region with higher oxide	Specimen cut	✓
30AD05	2,783	2,802	Fueled	HBU region	Mounted	✓
30AD05	3,240	3,259	Both	Highest oxide	Complete	✓
30AE14	653	672	TBD	Oxide thickness	✓	
30AE14	1,677	1,696	Defueled	Oxide thickness	Specimen cut	✓
30AE14	2,203	2,222	Defueled	HBU at oxide peak	Specimen cut	
30AE14	2,675	2,694	Both	HBU at oxide peak	Fueled complete, defueled specimen cut	✓
30AE14	3,399	3,418	Both	Highest oxide thickness	Complete	✓
3A1F05	1,260	1,279	Fueled	Oxide thickness	Complete	
3A1F05	1,585	1,604	Fueled	Oxide thickness	Complete	
3A1F05	2,006	2,025	Defueled	Oxide thickness	Specimen cut	✓
3A1F05	2,383	2,402	Defueled	HBU with higher oxide thickness, spalling oxide, pellet banding	Specimen cut	✓
3A1F05	2,735	2,754	Both	High oxide thickness at HBU	Complete	✓
3A1F05	3,105	3,124	Defueled	Peak oxide thickness	Defueled but unable to complete due to unexpected high dose rates	✓
3D8E14	700	719	Fueled	Oxide thickness	Mounted	
3D8E14	1,178	1,331	Fueled	Fretting mark depth (post fatigue test)	Mounted	
3D8E14	1,375	1,450	Fueled	Pellet-pellet gap and oxide thickness	Complete	✓
3D8E14	2,303	2,322	Defueled	Oxide thickness	Specimen cut	
3D8E14	2,655	2,674	Defueled	HBU with oxide spike	Complete	✓
3D8E14	3,206	3,225	Both	Highest oxide thickness	Fueled mounted/ defueled complete	✓
3F9N05	700	719	Defueled	Oxide thickness	✓	
3F9N05	1,425	1,444	Defueled	Oxide thickness	Specimen cut	✓
3F9N05	2,300	2,329	Defueled	Oxide thickness	Mounted	
3F9N05	2,863	2,882	Defueled	HBU with higher oxide	Complete	✓
3F9N05	3,331	3,350	Both	Peak oxide thickness and spalling oxide	Complete	✓
6U3K09	2,616	2,635	Fueled	CIRFT correlating data	Complete	
6U3K09	3,506	3,525	Fueled	CIRFT correlating data	✓	
F35P17	911	930	TBD	Oxide thickness	✓	
F35P17	1,300	1,319	Defueled	Oxide thickness	Specimen cut	✓
F35P17	2,008	2,027	TBD	HBU with higher oxide thickness	✓	
F35P17	2,383	2,402	Defueled	Oxide thickness, spalling oxide	Specimen cut	
F35P17	2,735	2,754	Both	Oxide thickness and spalling oxide	Complete	✓
F35P17	3,050	3,069	Both	Peak oxide thickness and spalling oxide	✓	✓

✓ Planned but not yet started.

Table B-4. Summary of metallographic section measurements obtained to date.

The data provided within the table is based upon multiple measurements of the feature taken from the same metallographic image at different radial locations. Shaded cells indicate that no measurement is available for the specimen image at this time. An asterisk (*) indicates an average value based upon only 2 measurements of that feature from the image. Some features were also measured nondestructively as reported by Montgomery [B-4] and comparisons are provided in Table B-5. Some METs were imaged but not measured, and they are not included in this table.

Rod ID and original section elevations (mm)			Cladding type	Heat-treated rod?	Estimated local burnup (GWd/MTU)	Average measured cladding thickness	Maximum measured	Minimum measured	Measured waterside oxide thickness	Maximum measured	Minimum measured	Measured Pellet side oxide thickness	Maximum measured	Minimum measured	Measured HBU rim thickness	Maximum measured	Minimum measured	Average measured Rod Outer diameter	Maximum measured	Minimum measured	Measured Cladding Inner diameter	Maximum measured	Minimum measured
						µm												mm					
30AD05	3240	3259	M5	No	55	541	546	535	12	13	11	11	14	7	57	70	43	9.389	9.416	9.374	8.279	8.288	8.273
30AE14	2675	2694	M5	Yes	61	560	575	541	9	10	8	13	18	10				9.389	9.416	9.374	8.279*	8.288	8.273
30AE14	3399	3418	M5	Yes	50	562	585	545	12	15	10	10	16	8	61	82	42	9.419	9.449	9.398	8.310	8.338	8.283
3D8E14	2655	2674	ZIRLO	No	64	549	564	531	34	41	31	15	18	12	70	108	52	9.466	9.495	9.424	8.330	8.344	8.306
6U3K09	2616	2635	ZIRLO	No	58	560	571	549	21	22	19	9	12	6	59	107	36	9.440	9.455	9.425	8.276	8.302	8.249
3F9N05	2863	2882	ZIRLO	Yes	58	554	563	547	30	38	24	12	16	8				9.450*	9.450	9.449	8.277*	8.277	8.275
3F9N05	3331	3350	ZIRLO	Yes	51	554	559	544	39	60	27	9	12	6	35	51	27	9.480*	9.496	9.464	8.271*	8.271	8.270
3A1F05	1260	1279	LT Zirc-4	No	56	560	565	555	15	18	14	10	12	7	54	74	43	9.436*	9.436	9.436	8.299*	8.299	8.299
3A1F05	2735	2754	LT Zirc-4	No	54	546	630	495	90	128	43	12	16	9	72	90	62	9.485*	9.548	9.421	8.290*	8.300	8.280
F35P17	2735	2754	Zirc-4	Yes	66	524	591	510	81	86	73	15	27	10	101	115	94	9.438	9.517	9.385	8.319	8.366	8.274

Table B-5. Comparison of Metallographic Section Measurements with Nondestructive Measurements

Rod ID and original section elevations (mm)			NDE measured (LVDT) local OD using LVDT (mm)	MET measured average OD (mm)	Differential OD (LVDT – MET) (mm)	NDE measured (eddy current) local waterside oxide thickness (µm)	MET maximum measured oxide thickness (µm)	Differential waterside oxide thickness (NDE – MET) (µm)	NDE measured (eddy current) wall thickness (µm)	MET measured wall thickness (µm)	Differential wall thickness (NDE-MET) (µm)
30AD05	3,240	3,259	9.420	9.389	0.031	20	13	7	572	541	31
30AE14	2,675	2,694	9.459	9.389	0.070	16	10	6	576	560	16
30AE14	3,399	3,418	9.440	9.419	0.021	23	15	9	574	562	12
3D8E14	2,655	2,674	9.517	9.466	0.051	42	41	1	570	549	21
6U3K09	2,616	2,635	9.474	9.440	0.034	22	22	0	566	560	6
3F9N05	2,863	2,882	9.482	9.450	0.032	45	38	7	564	554	9
3F9N05	3,331	3,350	9.478	9.480	-0.002	60	60	0	560	554	6
3A1F05	1,260	1,279	9.475	9.436	0.039	21	18	3	541	560	-19
3A1F05	2,735	2,754	9.564	9.485	0.080	137	128	9	490	546	-56
F35P17	2,735	2,754	9.549	9.438	0.111	88	86	2	503	524	-21

B-3.1 M5-Clad Sister Rods

Five MET views from three elevations are currently available for the two Phase 1 M5-clad sister rods—30AD05 (as received baseline condition), and 30AE14 (full-length rod heat treatment (FHT) applied), as shown in Figures B-4 through B-9. Rods 30AD05 and 30AE14 provide a good comparison because (1) they were from the same fuel assembly, (2) they were manufactured at the same time by the same fuel vendor, (3) they had the same irradiation history, and (4) they are only 5 GWd/MTU different in average burnup at the elevations examined.

The precipitated hydrides in the baseline M5-clad rod (30AD05) are homogeneously distributed through the thickness of the cladding and are oriented circumferentially. The pellet is cracked radially (as expected) with no missing pellet surface. The depth of the pellet HBU rim is 57 μm on average for the baseline rod (3,240–3,259 mm in elevation).

For the heat-treated M5-clad rod, many radial hydrides are visible, particularly at the inner diameter (ID) of the cladding. The radial hydrides appear to have preferentially precipitated at locations where a pellet crack exists at the cladding ID, as illustrated in Figure B-7's colorized view. The cladding is not supported by the pellet at the pellet crack, and this results in a higher local stress concentration. The higher stress field provides a preferential location for hydride precipitation. The pellet cracks are as expected, with no missing pellet surface. The HBU rim is 61 μm on average.

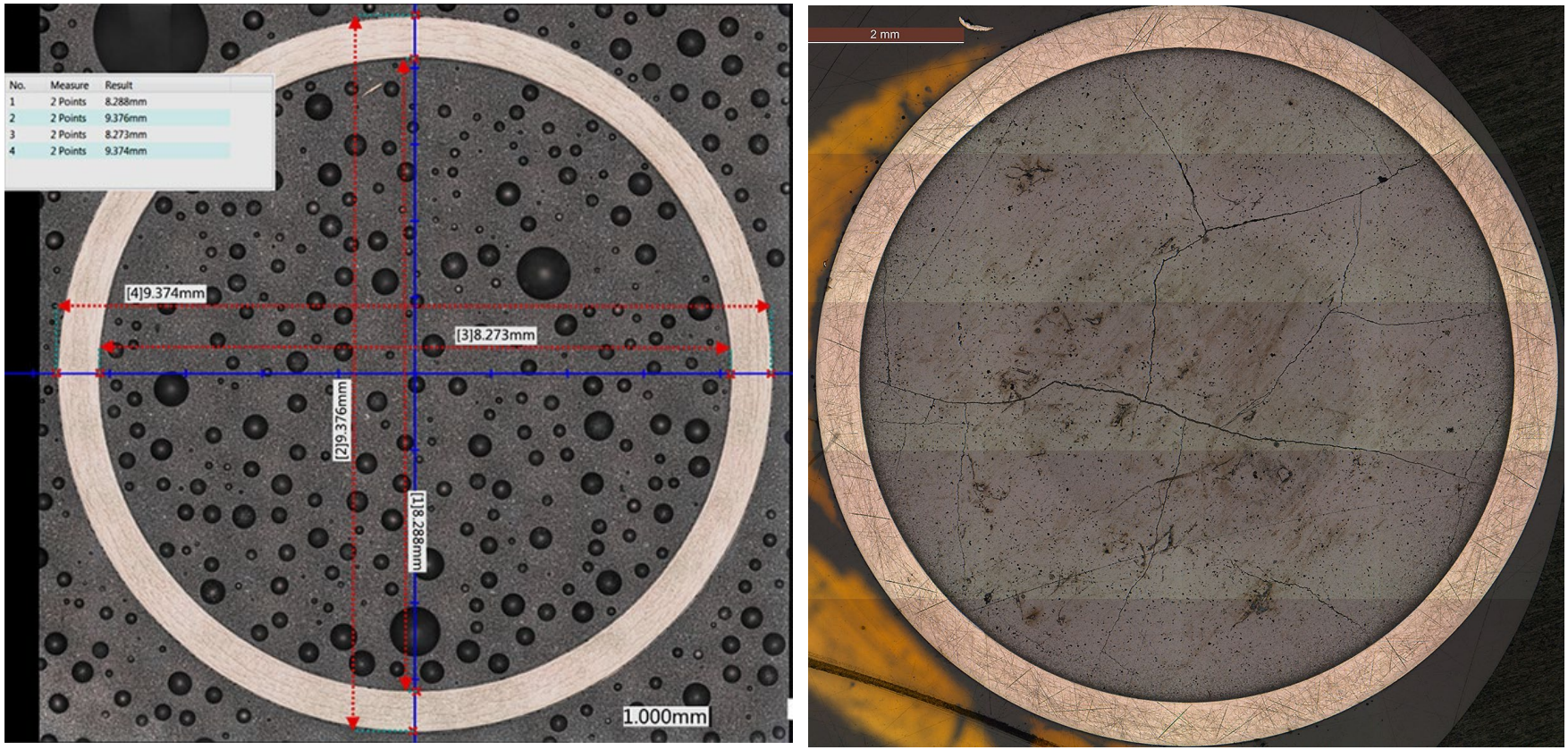

Figure B-4. Fueled (right) and defueled (left) overall section views, 30AD05-3240-3259 (baseline rod).

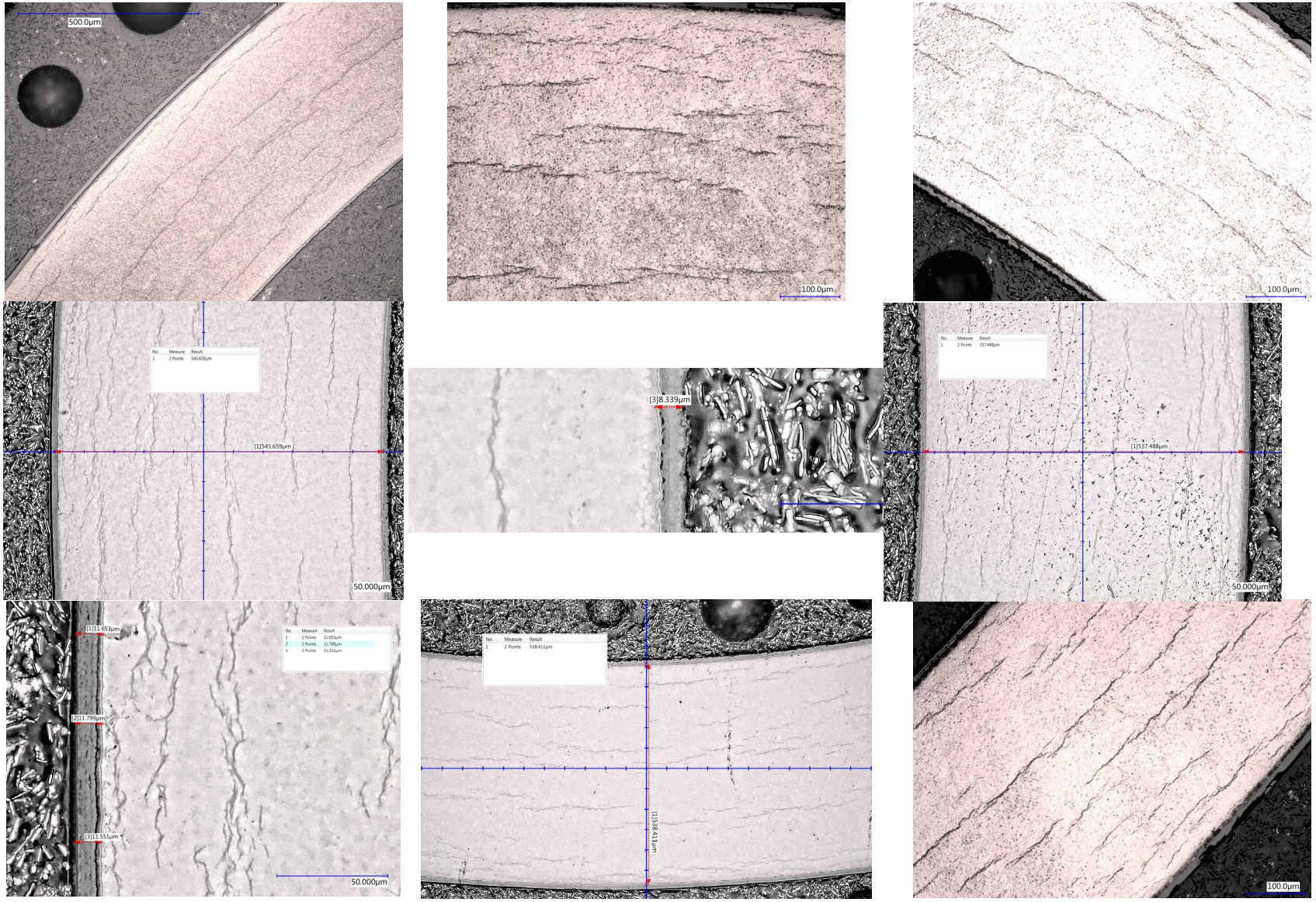

Figure B-5. Magnified areas of the cladding, 30AD05-3240-3259 (baseline rod).

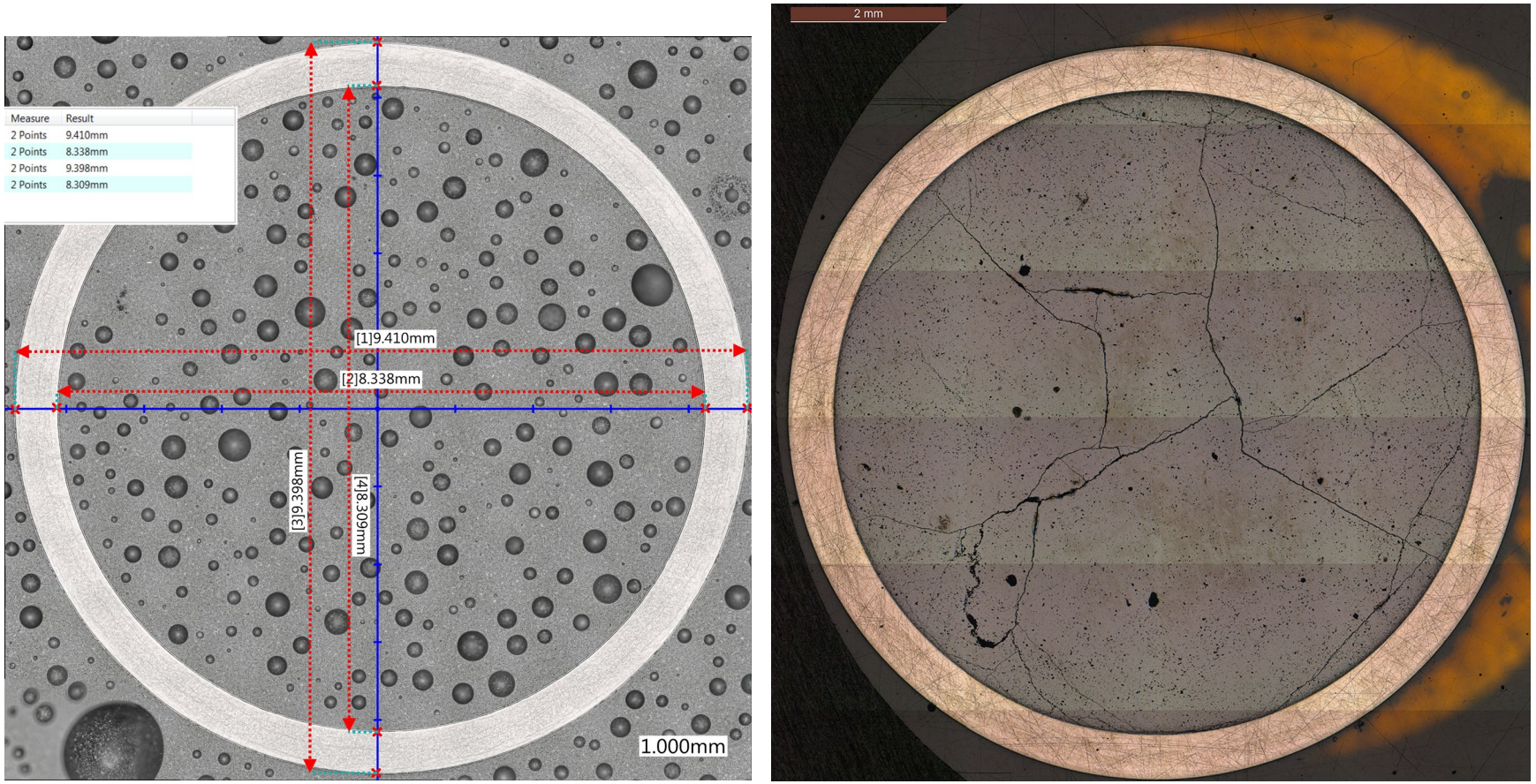

Figure B-6. Fueled (right) and defueled (left) overall section views, 30AE14-3399-3418 (heat-treated rod).

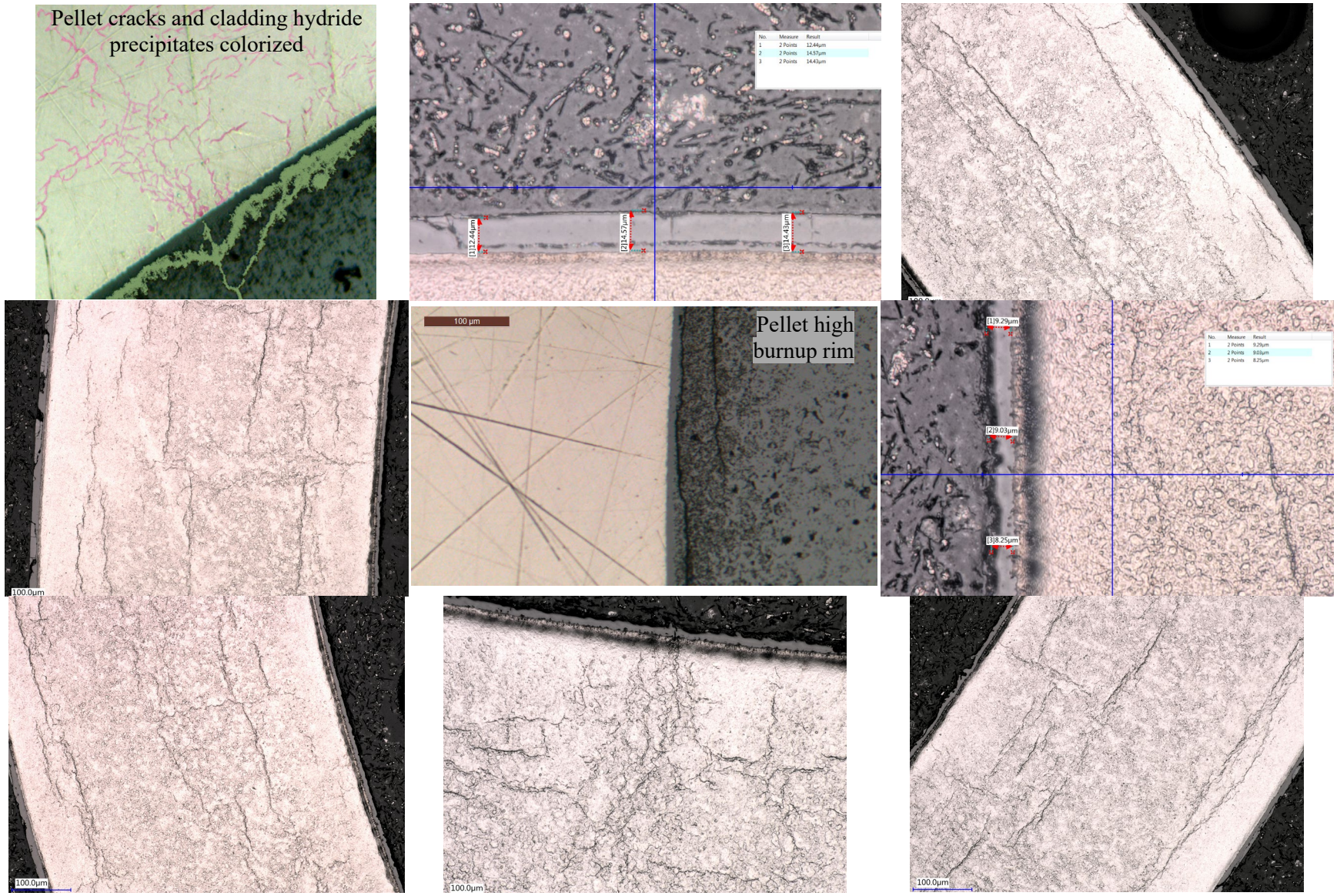

Figure B-7. Magnified views, 30AE14-3399-3418 (heat-treated rod).

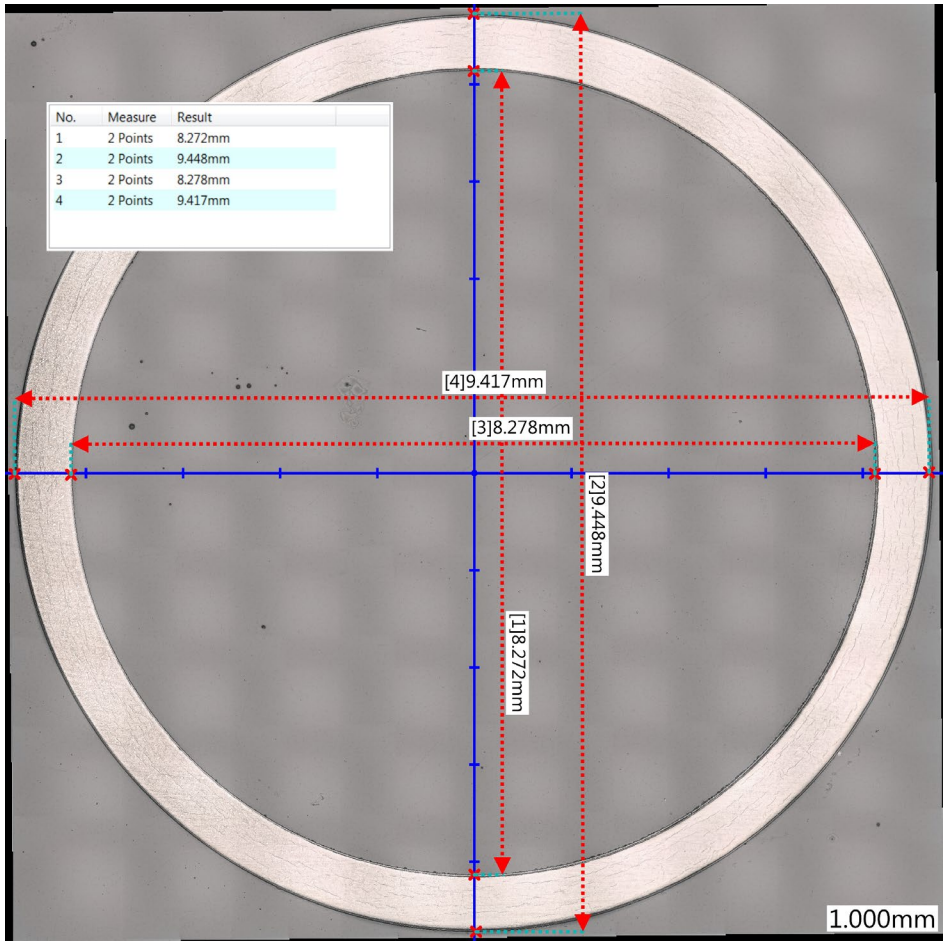

Figure B-8. Defueled overall view, 30AE14-2675-2694 (heat-treated).

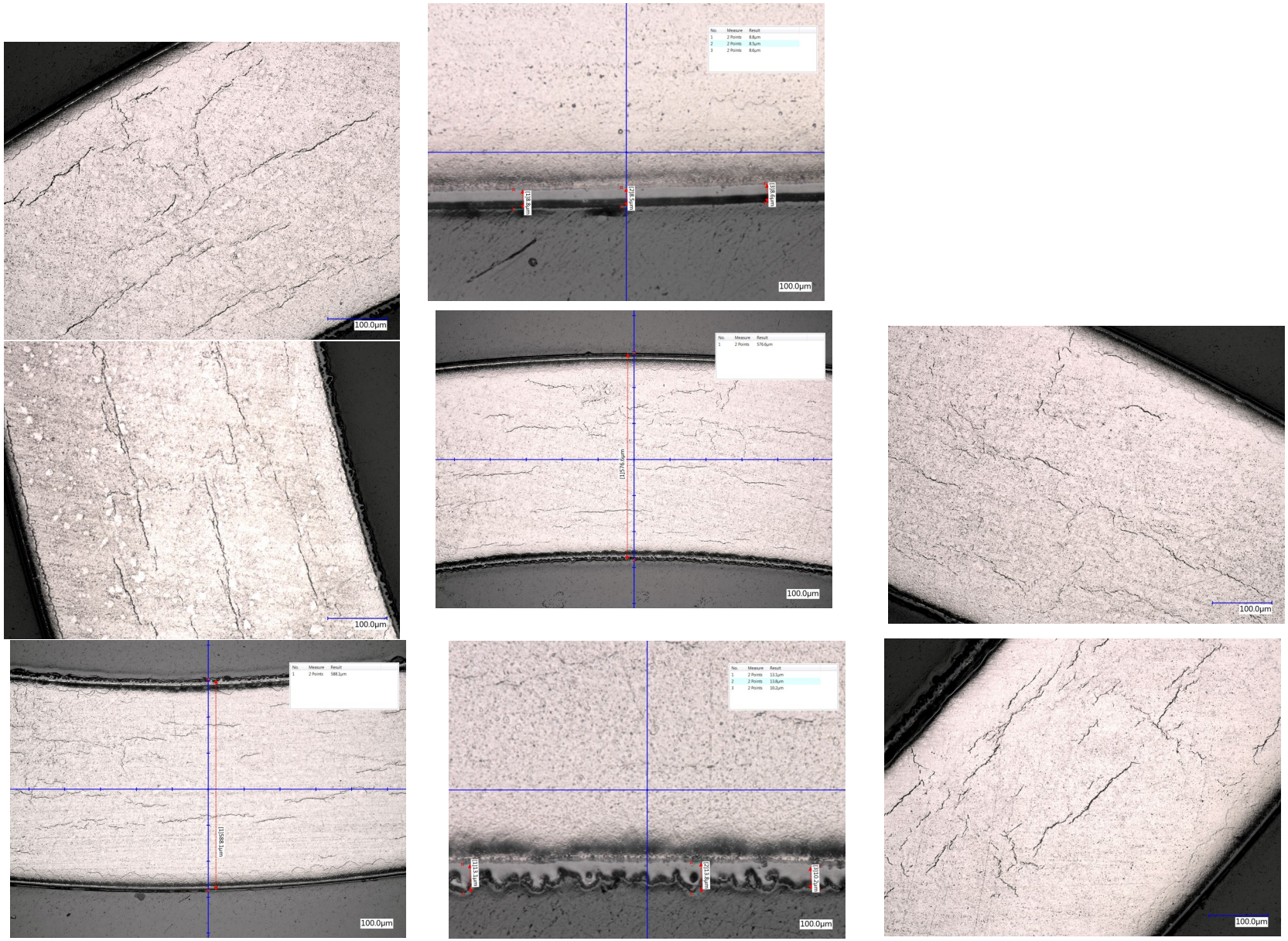

Figure B-9. Magnified areas of the cladding, 30AE14-2675-2694 (heat-treated).

B-3.2 ZIRLO-Clad Sister Rods

Eight MET mounts are available for the three Phase 1 ZIRLO-clad sister rods: 3D8E14 and 6U3K09 (as-received baseline rods) and 3F9N05 (FHT applied). Figures B-10 through B-14 provide views of the baseline rods, and Figures B-15 through B-19 provide views of the heat-treated rod. The three rods examined were from the same fuel vendor but were manufactured at different times and operated in different reactor cycles. At the elevations examined, the difference in estimated burnup ranges from 0 to 13 GWd/MTU (see Table B-4).

The precipitated hydrides in the baseline ZIRLO-clad rods (3D8E14 and 6U3K09) are primarily located at the OD and ID of the cladding and are oriented circumferentially. For 3D8E14, there are many short hydrides in the central region of the wall that form a cross pattern, and there are several relatively long radial hydrides located at the cladding ID, as shown in Figures B-11 and B-12. The rod 6U3K09 MET was not polished well enough to fully visualize the cladding hydrides, although there is a deeper OD field of circumferential hydrides (Figure B-14). The 6U3K09 pellet is cracked in the expected pattern, with no missing pellet surface visible. The depth of the pellet HBU rim is 59 μm on average for the baseline rod (2,616–2,635 mm in elevation).

For the heat-treated ZIRLO-clad rod, the circumferential hydrides are more regularly distributed through the wall section, as shown in Figures B-16 and B-19, perhaps indicating hydrogen migration during the heat treatment. Several radial hydrides are visible at the ID and near the OD of the cladding. Because the polish on the fueled MET is not fine enough to fully visualize all of the hydrides, it is difficult to assess the preference for hydride precipitation at pellet crack locations. However, an inspection of magnified areas of the fueled MET (provided in Figure B-17) seems to indicate radial hydrides at pellet crack locations. This MET will be further processed and etched to better highlight the hydrides. The pellet cracks are as expected, with no messing pellet surface. The HBU rim is 35 μm on average.

A pellet-pellet gap of 3 mm was identified at an elevation of 1,403 mm during the NDE [B-4]. The rod was sectioned longitudinally at that elevation to reveal the pellet-pellet interfaces and the gap and to allow for additional examination of the pellet and cladding condition as related to the gap. A longitudinal slice of the section (approximately one third of the rod OD) was removed to reveal the pellets and was reserved for cladding hydrogen measurements. The resulting segment was then mounted and polished, and the gap was measured optically, as shown in Figure B-20. The gap is actually less than 1 mm, as shown in Figure B-20(a), and was overestimated by the gamma scan, likely due to the reduced gamma source at the chamfers and dishes in the pellets. The longitudinal specimen is slightly tilted in its mount, giving the appearance of a taper, as shown in Figure B-20(b). Because of the tilt and the off-center cut location, diameter measurements taken from the longitudinal image are not accurate. Axial measurements taken from the longitudinal image are less affected but are still inaccurate. The longitudinal view allows for inspection of both axial and radial pellet cracks that occurred during reactor operation. The pellet HBU rim is easily discernable and is enhanced at the pellet chamfer locations. The lower pellet has a small chip that relocated within the dish region, as shown at the left end of Figure B-20(b). At least one chamfer has loose chips, as shown at the right end of Figure B-20(b). Figure B-21 provides closer views of these details and provides a view of the hydride distribution just inside the cladding ID. The ID cladding oxide layer is discontinuous at the pellet-pellet gaps, and although some pellet material appears to be well bonded with the cladding ID oxide, there is a continuous crack in the pellet that keeps the pellet and cladding from fully functioning as a solid mechanical section. Following axial imaging, the specimen was cross sectioned to allow views in the gap (Figure B-20[d]) and above (Figure B-20[e]) and below it (Figure B-20[c]). The OD, ID, oxide layers, cladding wall thickness, and pellet HBU rim were measured on the cross-sectional METs and are provided in Table B-6. For comparison, the intact rod OD measured during NDE using LVDTs is also listed in Table B-6. The pre-cut OD matches within 4 μm in the pellet elevations, but after cutting, the MET-measured OD in the gap region is 8.8 μm larger. It is not clear whether some residual strain was released in the gap after cutting or whether this discrepancy is caused by

measurement uncertainty. Figure B-21 provides examples of the hydride distribution in the cladding (a) above the gap in the pellet body, (b) in the gap, and (c) below the gap in the pellet body. Although the section above the gap was not fully polished and the central portion of the wall is thus not useful for comparison, there is not a visual difference in the hydride distribution in the gap as compared with the cladding in the pellet body region. Total cladding hydrogen measurements will be performed to better quantify any additional hydrogen (in solution or precipitated) in the pellet-pellet gap region.

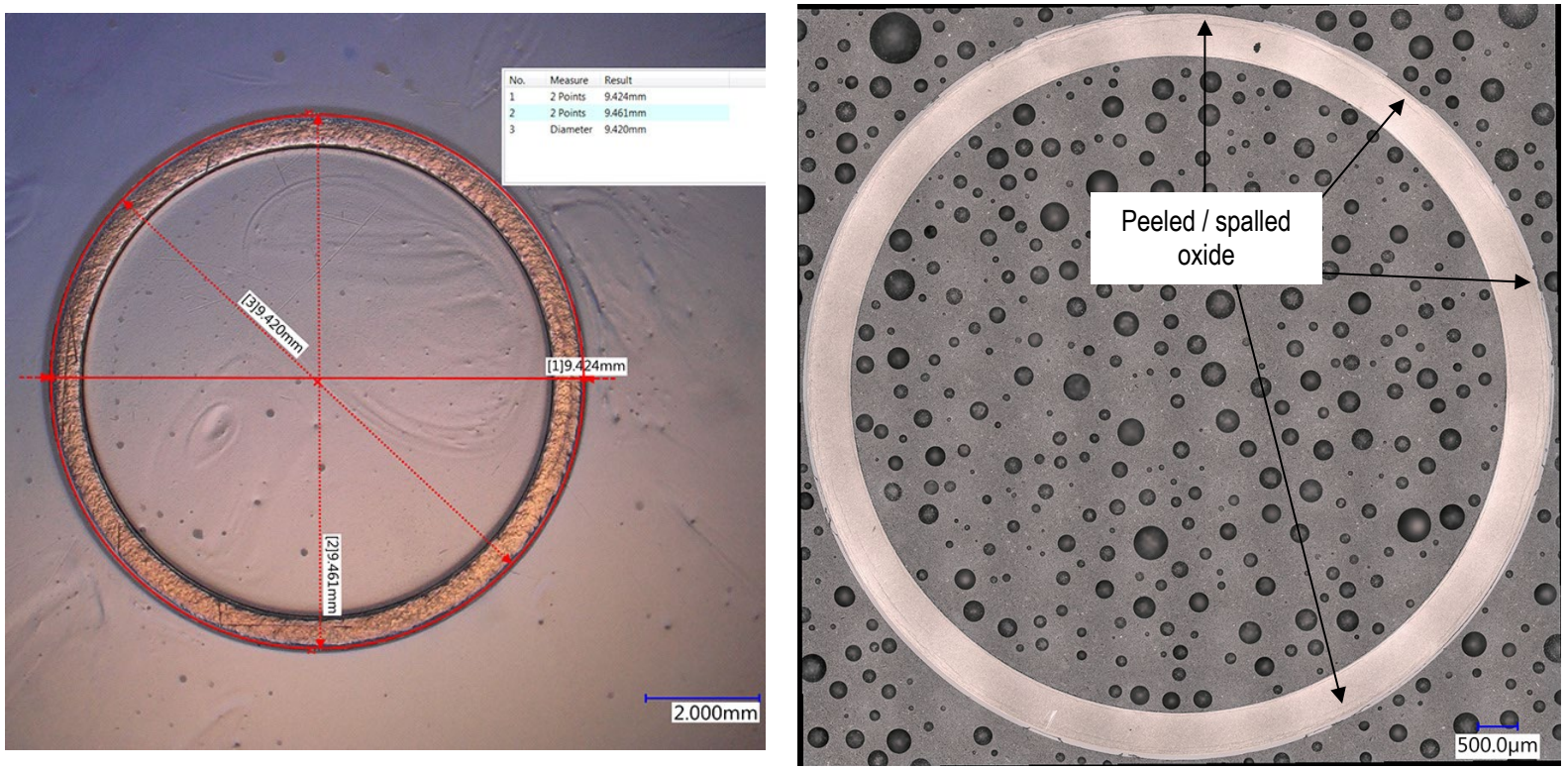

Figure B-10. Defueled overall view, 3D8E14-2655-2674 (left) and 3D8E14-3206-3225 (right) (baseline rod).

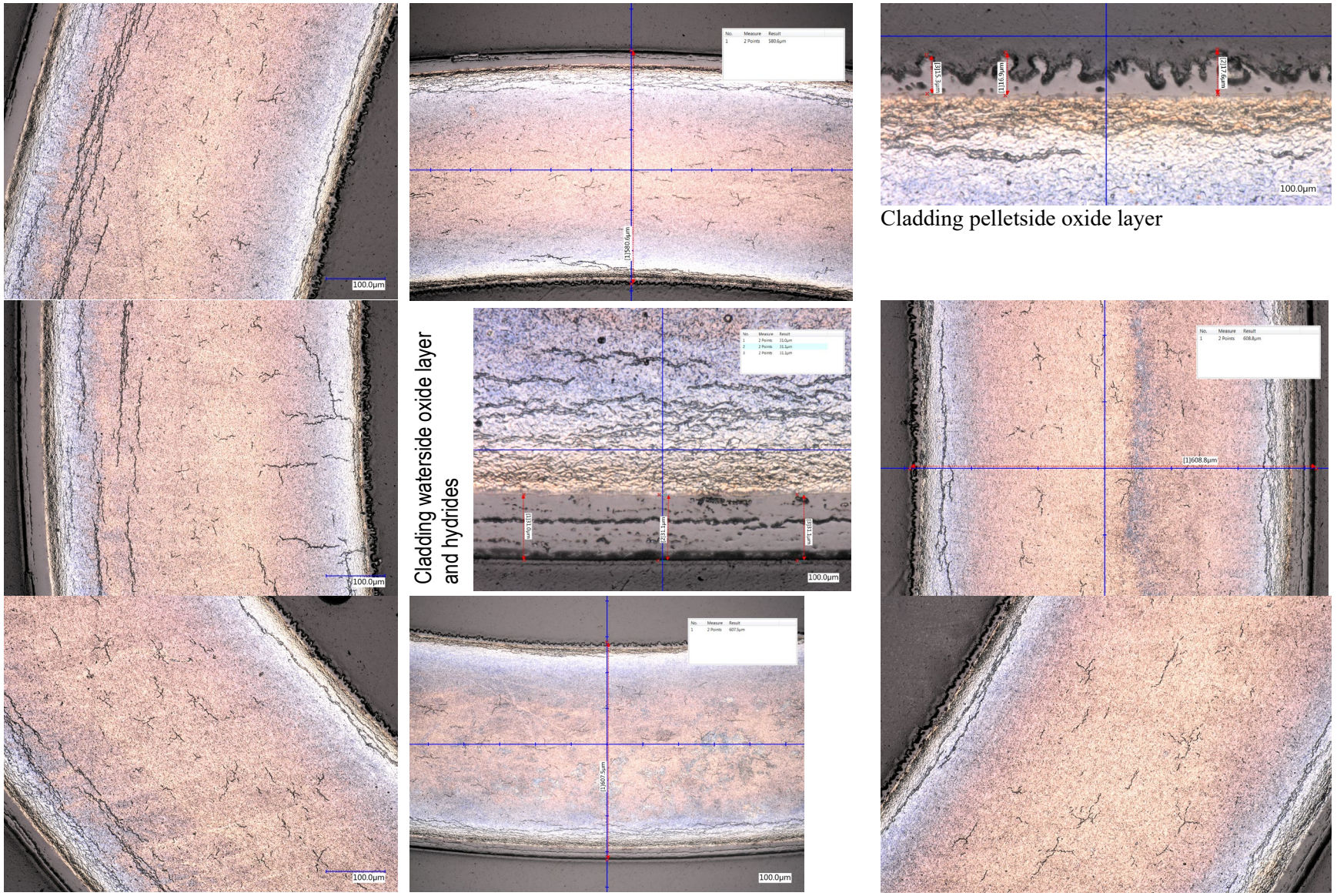

Figure B-11. Magnified areas of 3D8E14-2655-2674 (baseline rod).

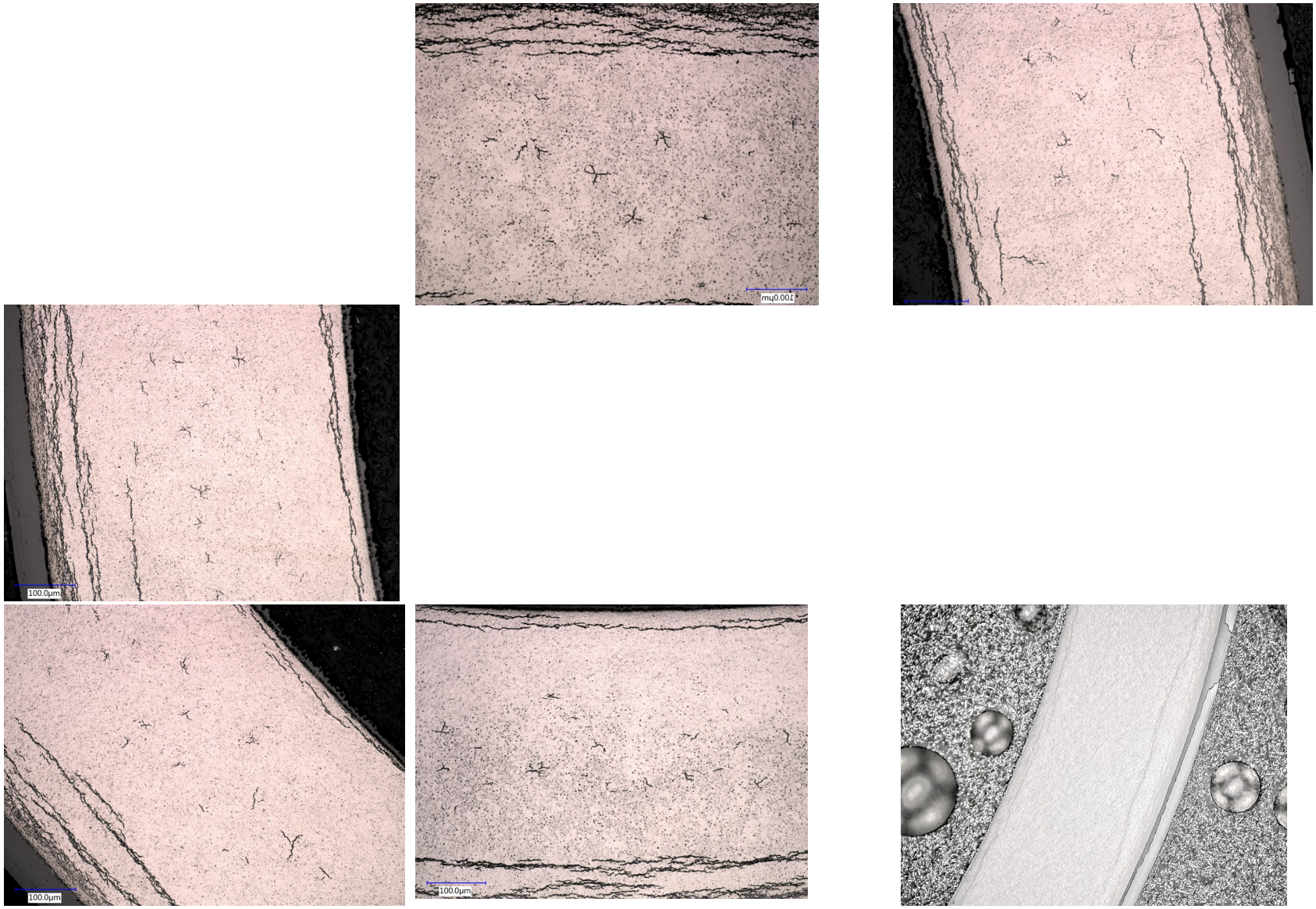

Figure B-12. Magnified areas of 3D8E14-3206-3225 (baseline rod).

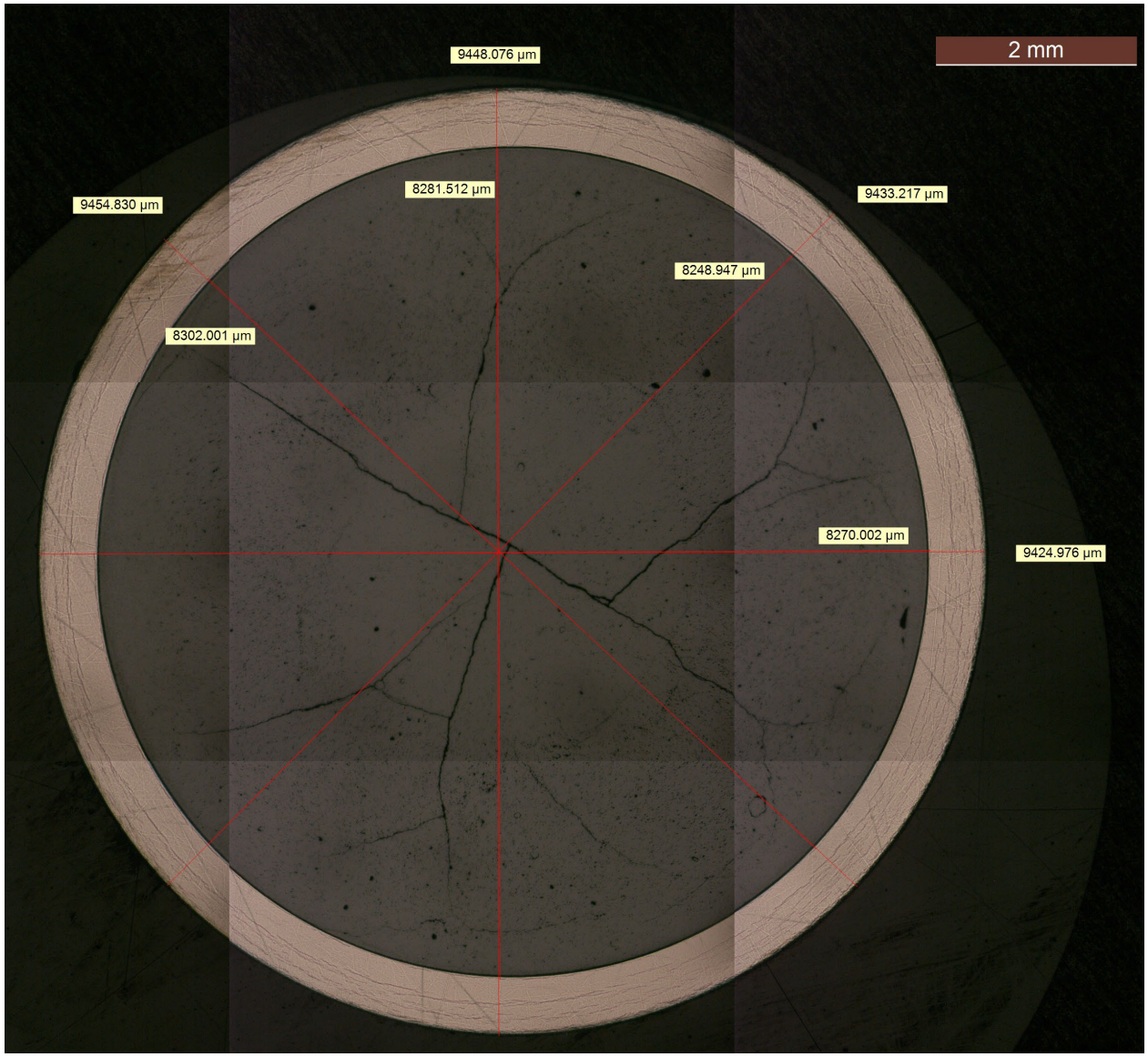

Figure B-13. Fueled overall view, 6U3K09-2616-2635 (baseline rod).

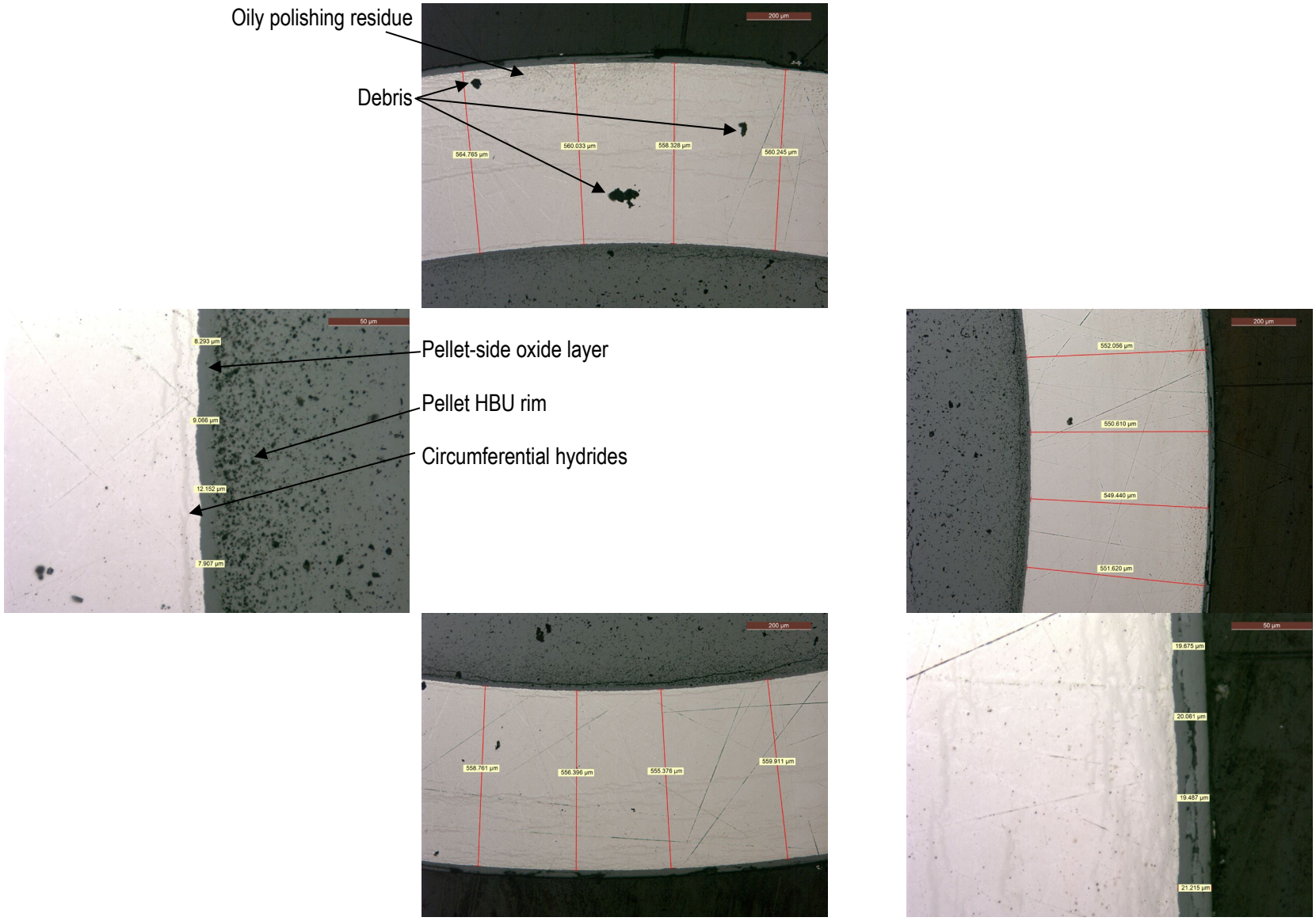

Figure B-14. Magnified views, 6U3K09-2616-2635 (baseline rod).

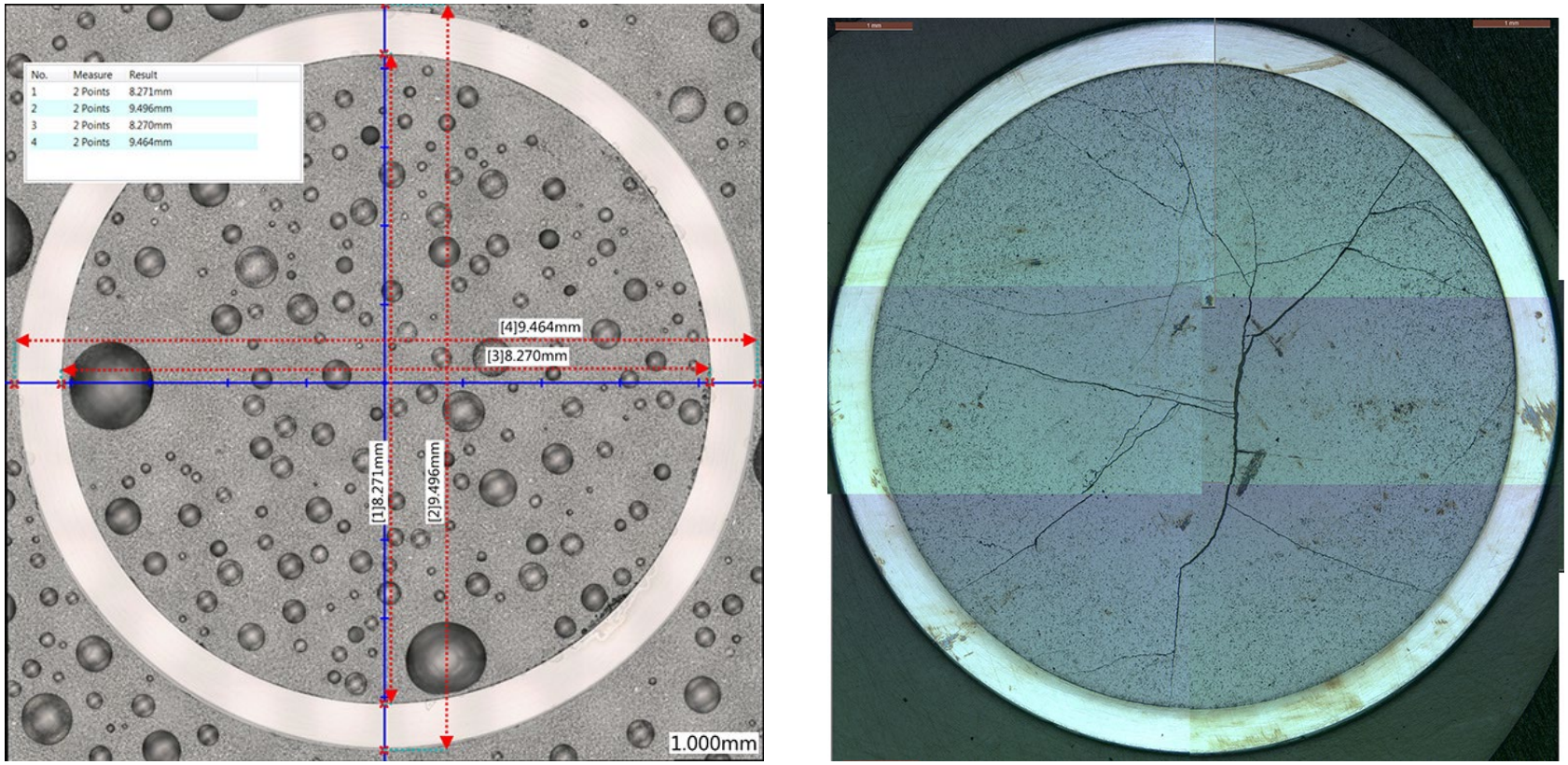

Figure B-15. Defueled (left) and fueled (right) overall views of 3F9N05-3331-3350 (heat-treated).

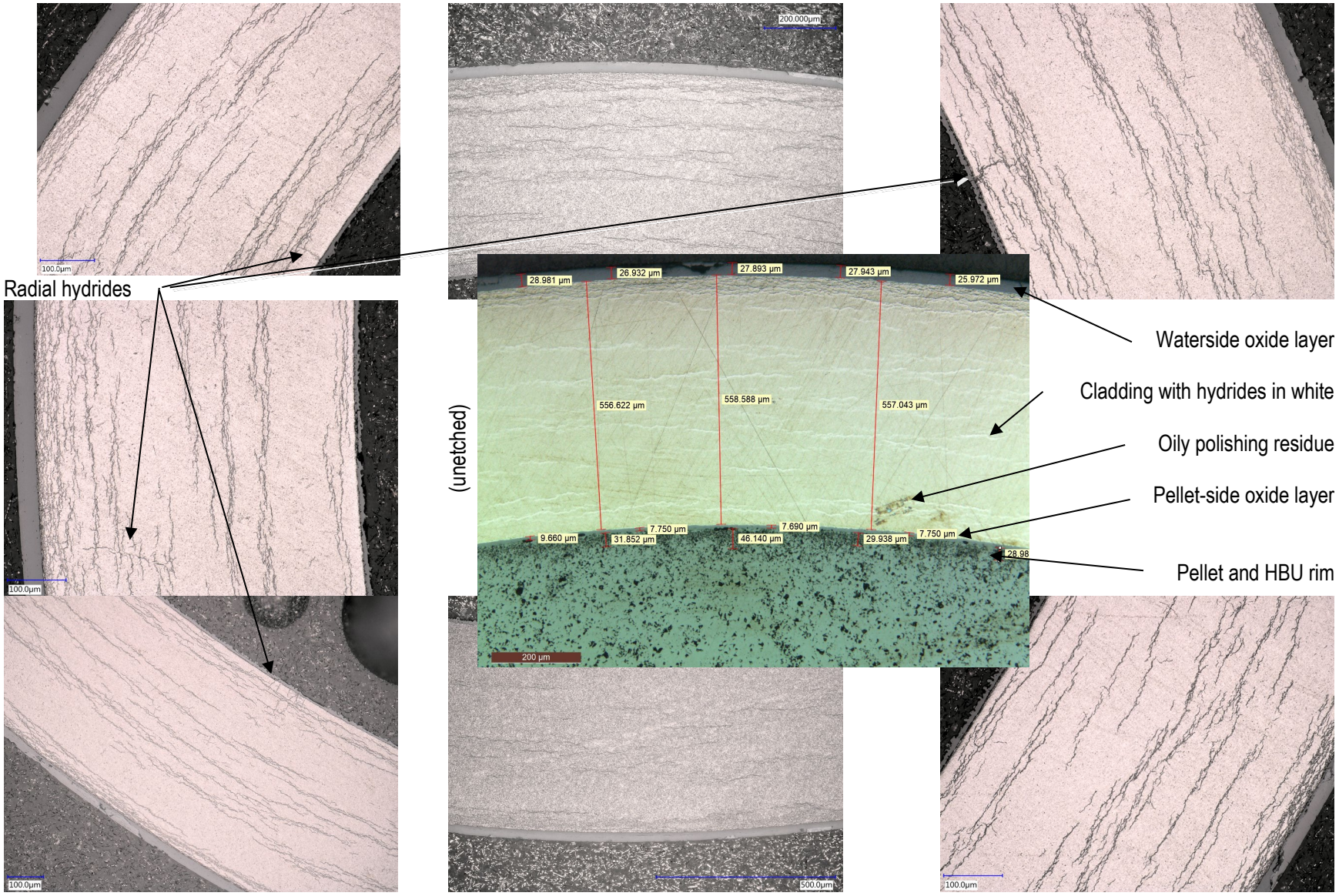

Figure B-16. Magnified views of 3F9N05-2863-2882 (heat-treated).

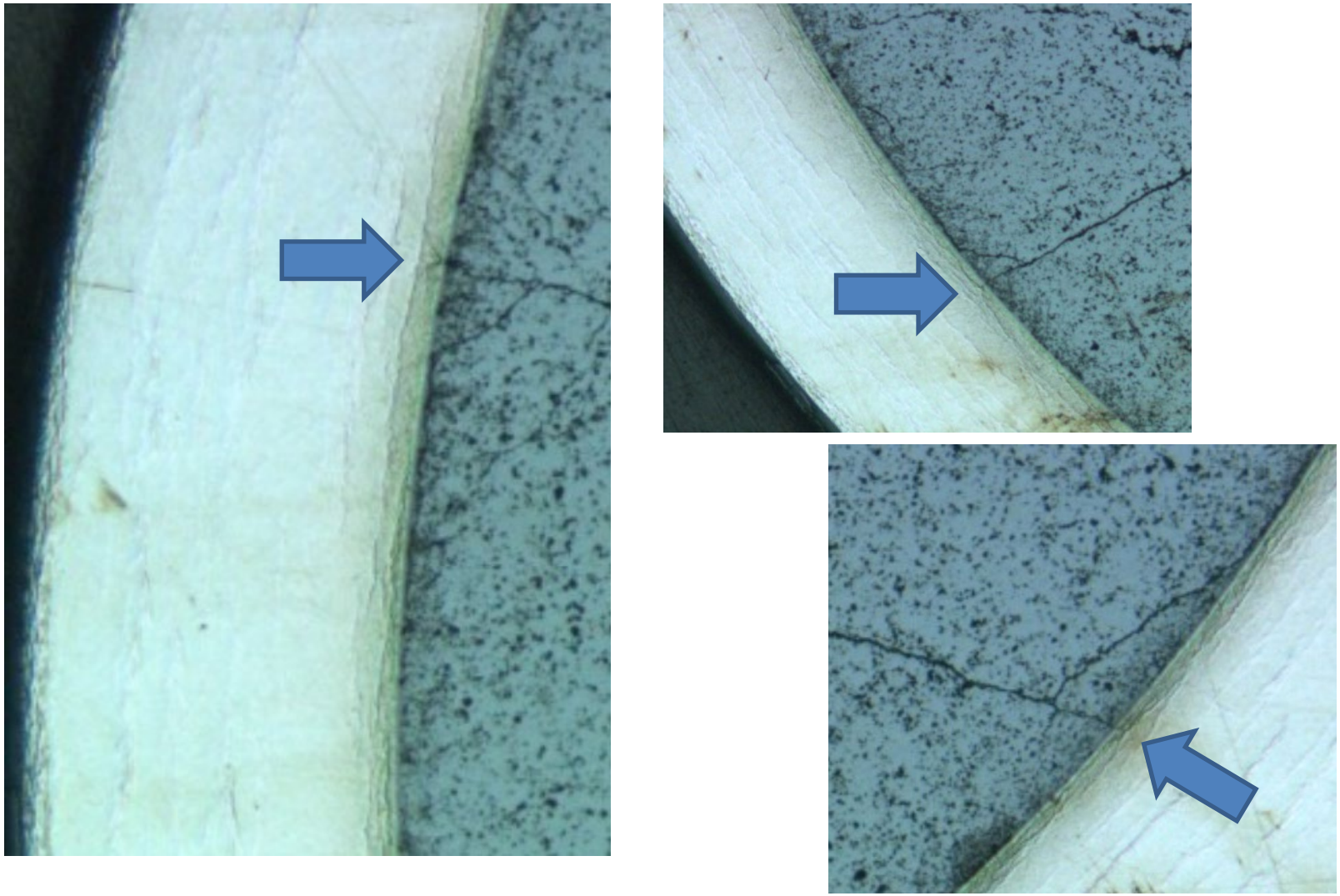

Figure B-17. Magnified views of 3F9N05-2863-2882 (heat-treated) with cladding at pellet crack locations indicated.

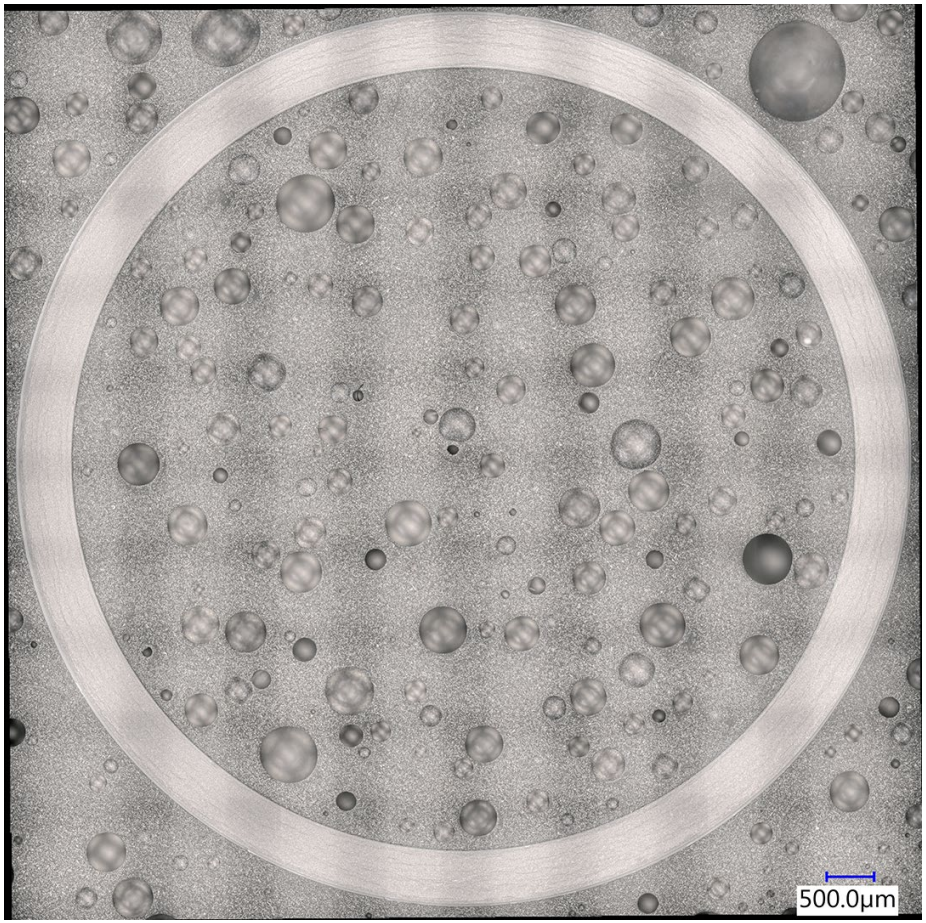

Figure B-18. Defueled overall view of 3F9N05-2863-2882 (heat-treated).

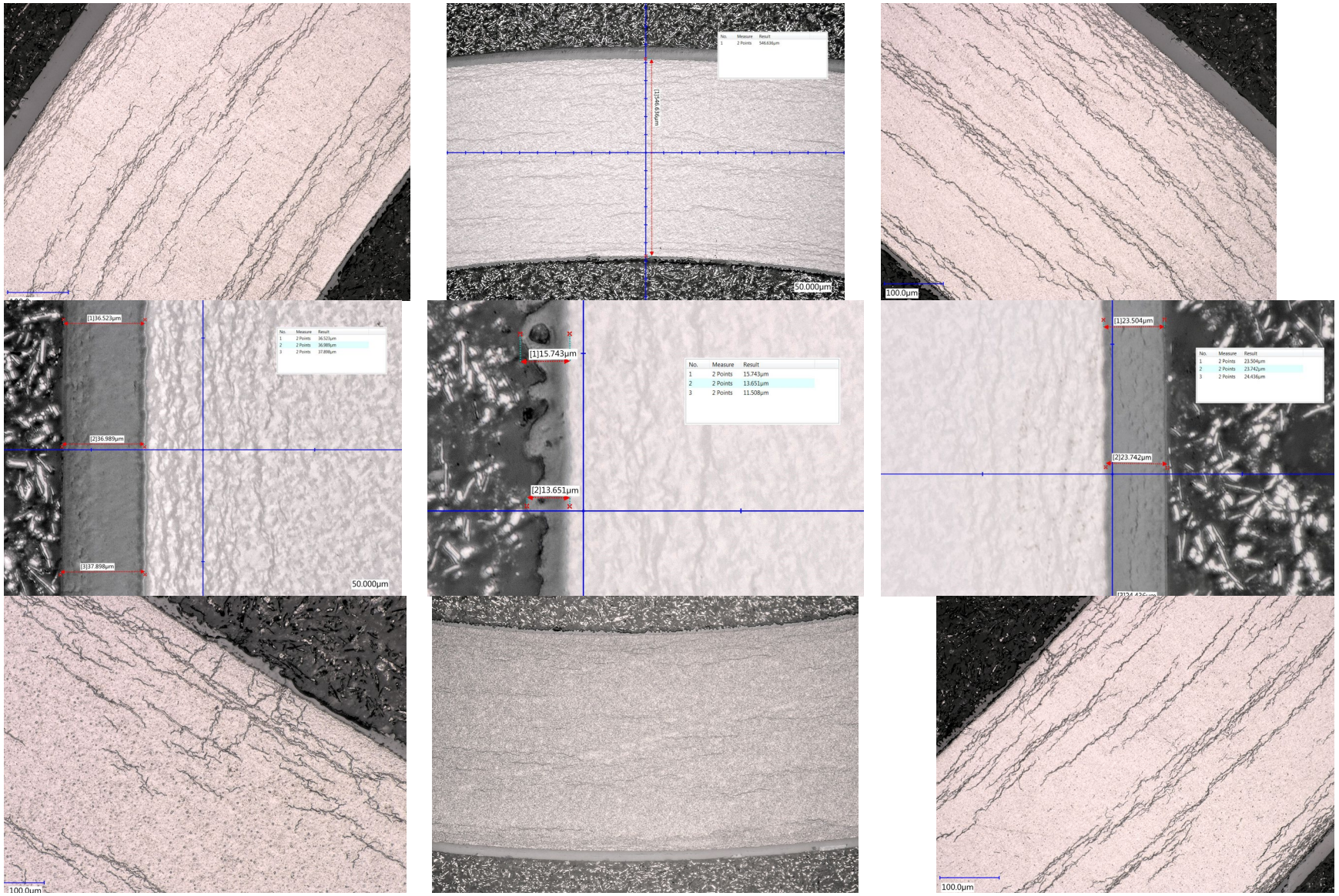

Figure B-19. Magnified views of 3F9N05-2863-2882 (heat-treated).

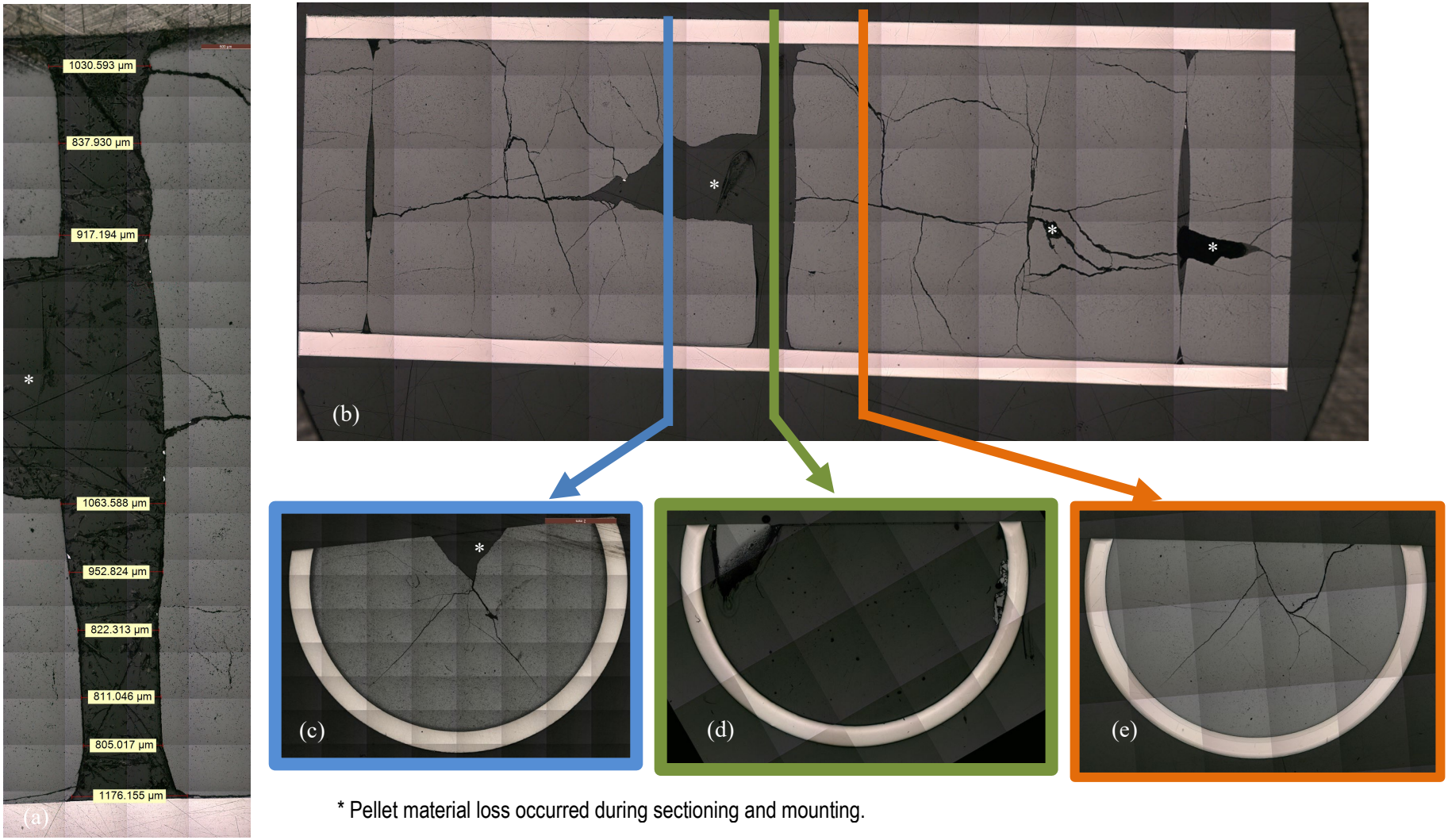

Figure B-20. 3D8E14 at 1,403 mm elevation: (a) pellet-pellet gap measurements, (b) longitudinal section view and cross-sectional view locations, (c) cross-sectional view of pellet below the pellet-pellet gap, (d) cross-sectional view in the pellet-pellet gap, and (e) cross-sectional view of the pellet above the pellet-pellet gap.

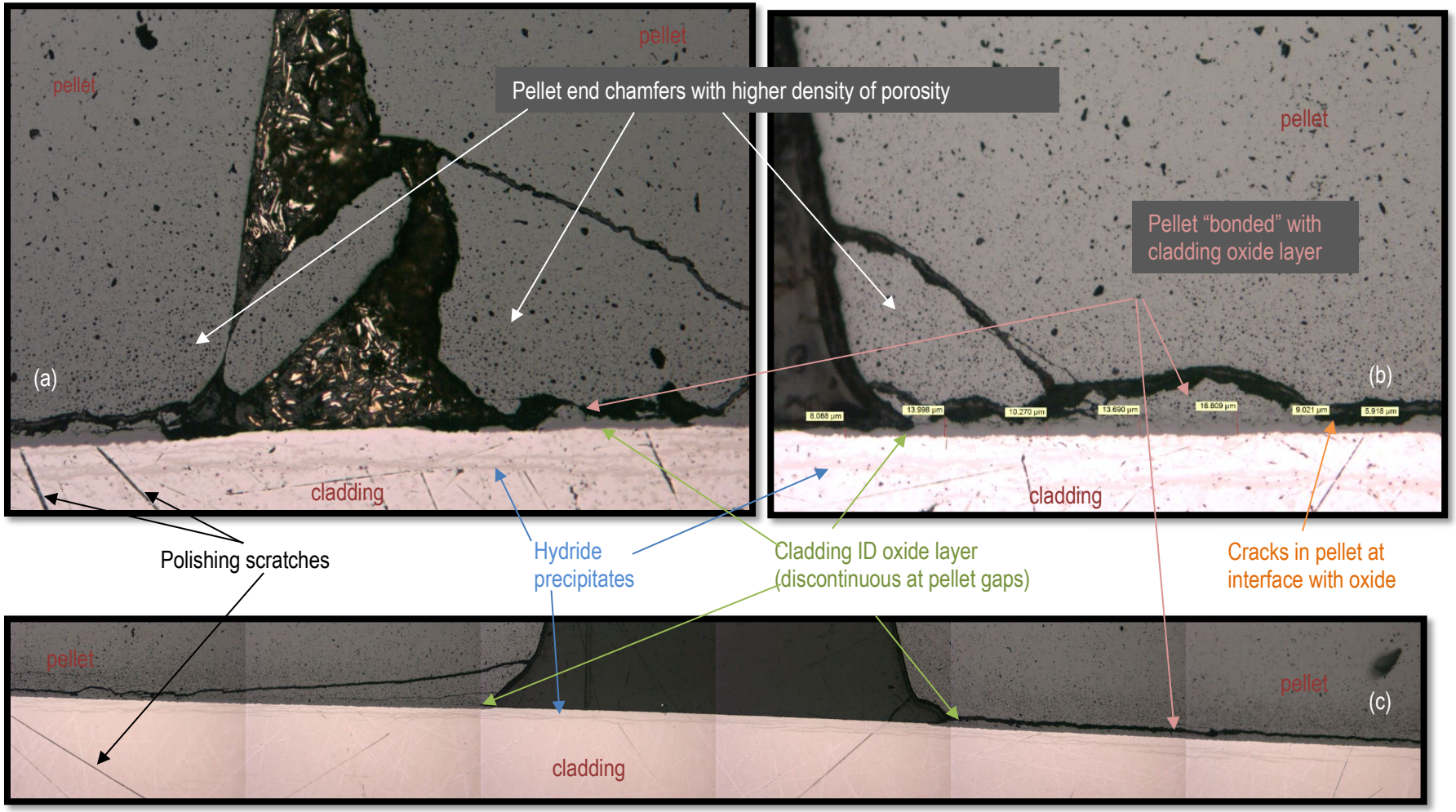

Figure B-20 3D8E14 centered at 1,403 mm elevation 200× longitudinal views of three pellet-pellet interface locations showing pellet cracking, HBU rim and corner effects, and cladding ID hydrides.

Table B-6. Measurements of 3D8E14 centered at 1,403mm elevation.

	Cladding wall thickness (µm)			Waterside oxide layer thickness (µm)			Pellet-side oxide layer thickness (µm)			Pellet HBU rim thickness (µm)			Cladding ID (µm)	Cladding OD (µm)	NDE average OD (µm)
	Average	Maximum	Minimum	Average	Maximum	Minimum	Average	Maximum	Minimum	Average	Maximum	Minimum			
Above gap (~1,408 mm elevation)	568.9	580.2	558.6	14.9	18.3	12.5	11.2	13.7	6.2	85.8	108.0	65.0	8,318.0	9,480.2	9,481.9
In gap (~1,403 mm elevation)	568.3	576.9	556.9	12.0	12.4	11.6	0	0	0	N/A			8,363.3	9,475.5	9,466.4
Below gap (~1,398 mm elevation)	569.7	582.9	558.2	12.9	15.6	9.2	11.7	17.5	7.9	85.1	130.5	61.5	8,339.4	9,483.4	9,480.0

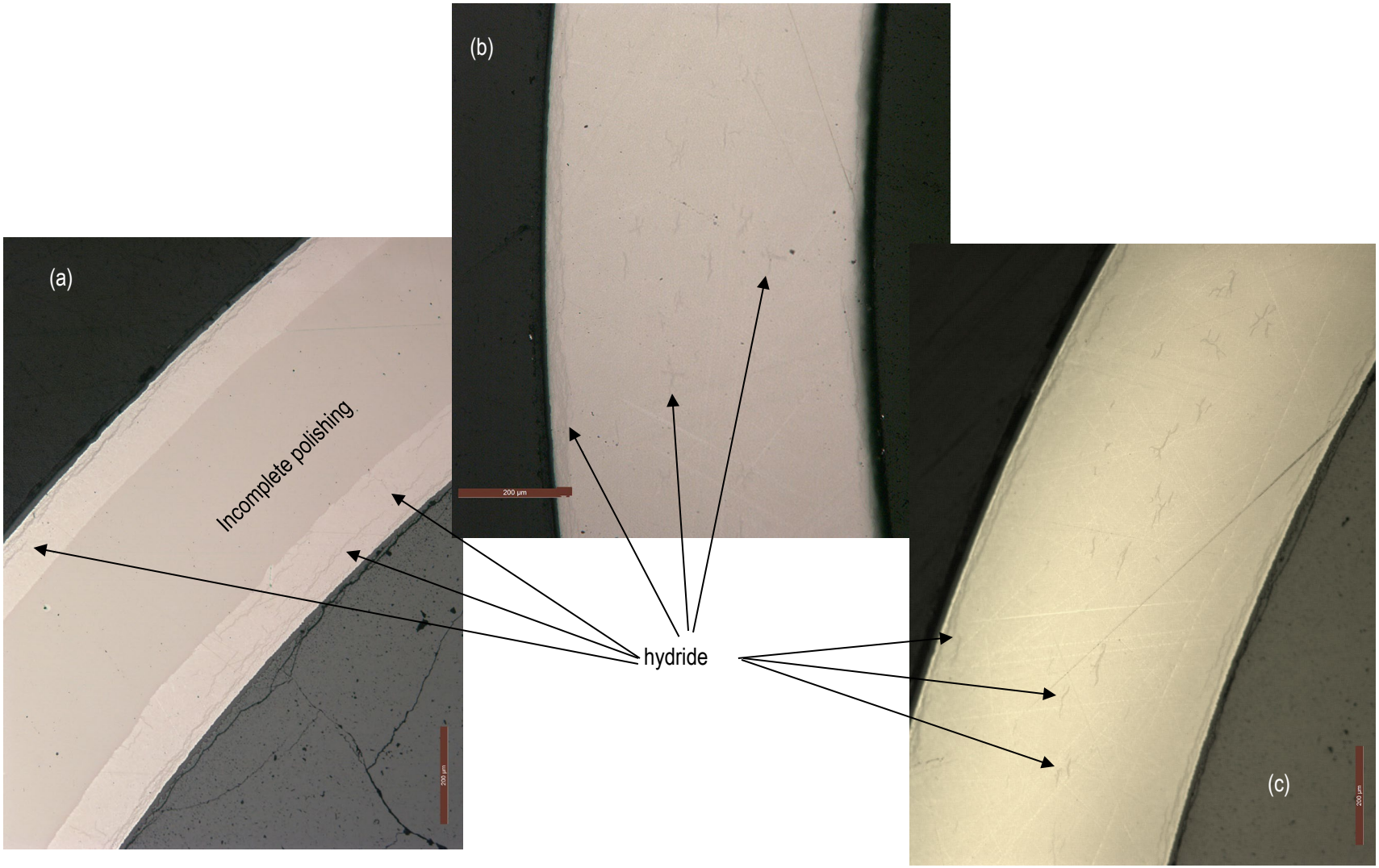

Figure B-21. 3D8E14 centered at 1,403 mm elevation, cladding hydride distribution (a) above the gap in the pellet body, (b) in the gap, and (c) below the gap in the pellet body.

B-3.3 Zirc-4-Clad Sister Rods

Figures B-22 through B-24 provide views of F35P17-2735-2754 (heat-treated). Two MET views from one elevation are available for the Phase 1 Zirc-4-clad sister rods. Numerous circumferential hydrides are visible throughout the thickness of the cladding. The visible radial hydrides are short. A large portion of the waterside oxide layer is spalled, with an average waterside oxide layer thickness of 81 µm and a maximum thickness of 86 µm at this rod elevation. The spalled layer is almost the full thickness, as shown in Figure B-23, with a ~9 µm layer remaining in the spalled area. The remaining wall thickness in the spalled area is ~510 µm. The pellet cracks are as expected with no missing pellet surface. The pellet HBU rim is 101 µm on average.

F35P17 was manufactured by Westinghouse and was used in a lead rod program. It was operated to a rod average burnup of 60 GWd/MTU, and the waterside oxide thickness was previously measured at poolside after reactor discharge [B-9]. The waterside oxide thickness was also measured during the sister rod NDE (before the heat-treatment) using two different instruments, the Electric Power Research Institute's F-SECT system, and ORNL's eddy current system. At the elevation of F35P17-2735-2754, F-SECT reported ~90 µm, and the eddy current reported ~100 µm.

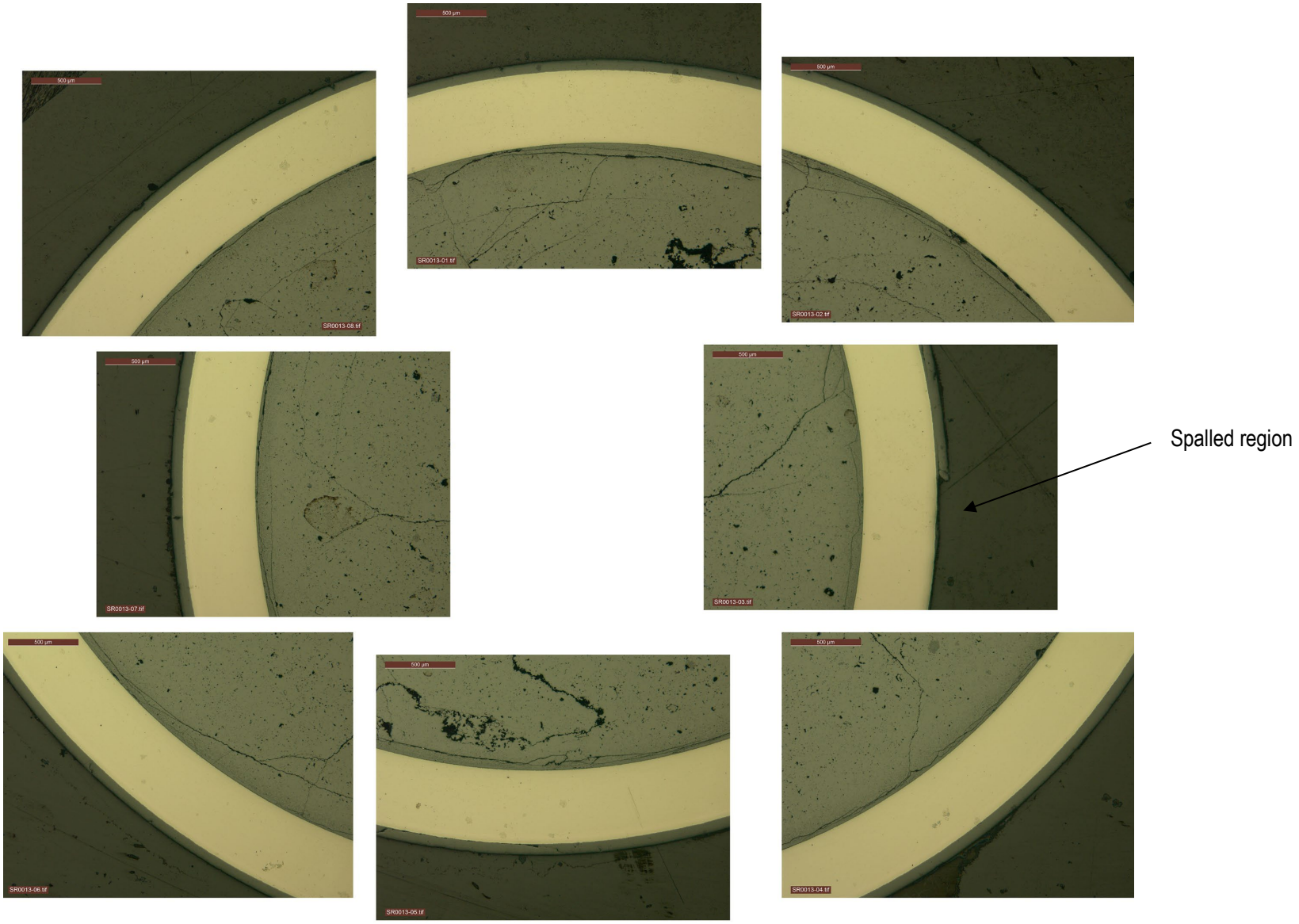

Figure B-22. Mosaic view, fueled, F35P17_2735_2754 (heat-treated).

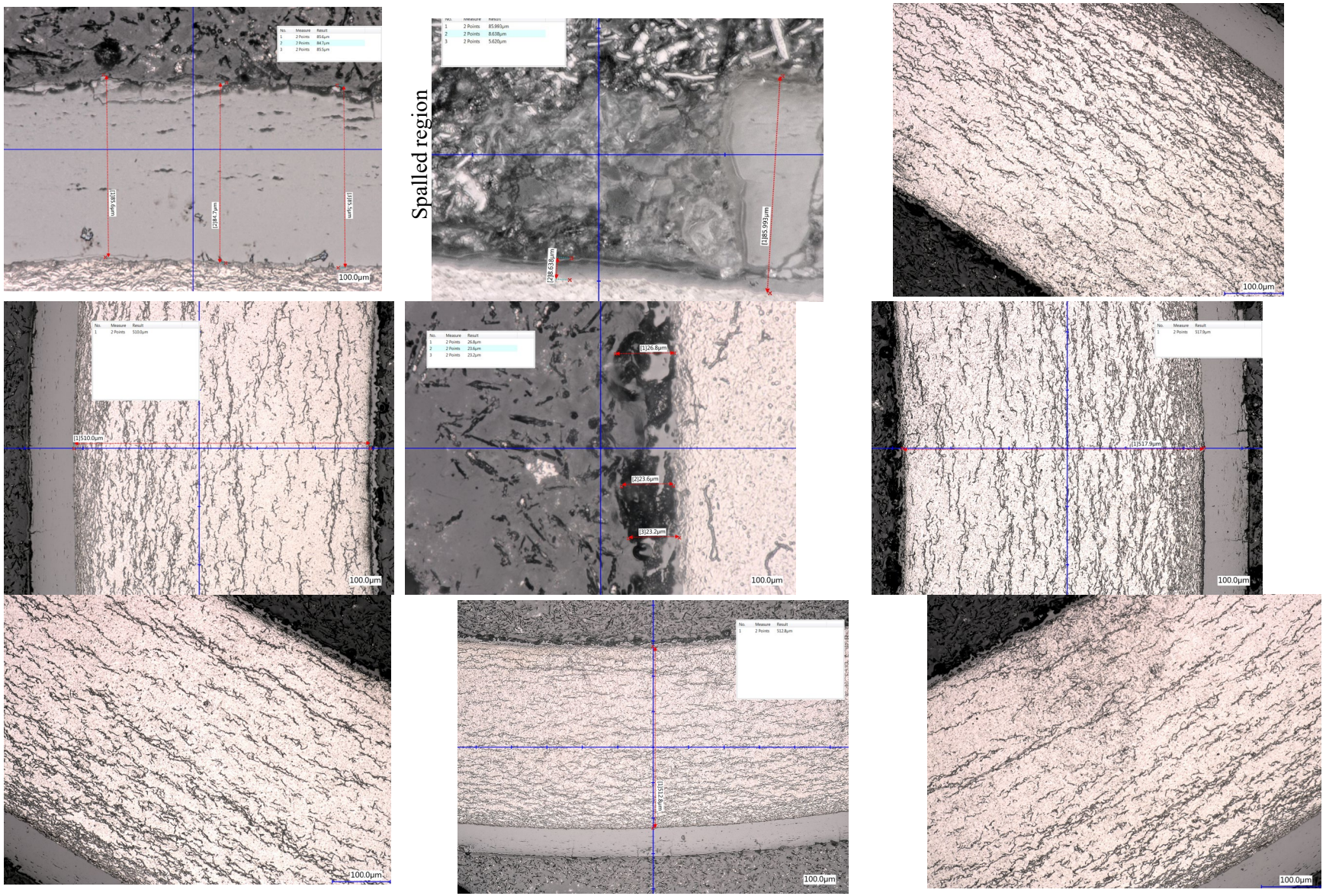

Figure B-23. Magnified views, defueled, F35P17-2735-2754 (heat-treated).

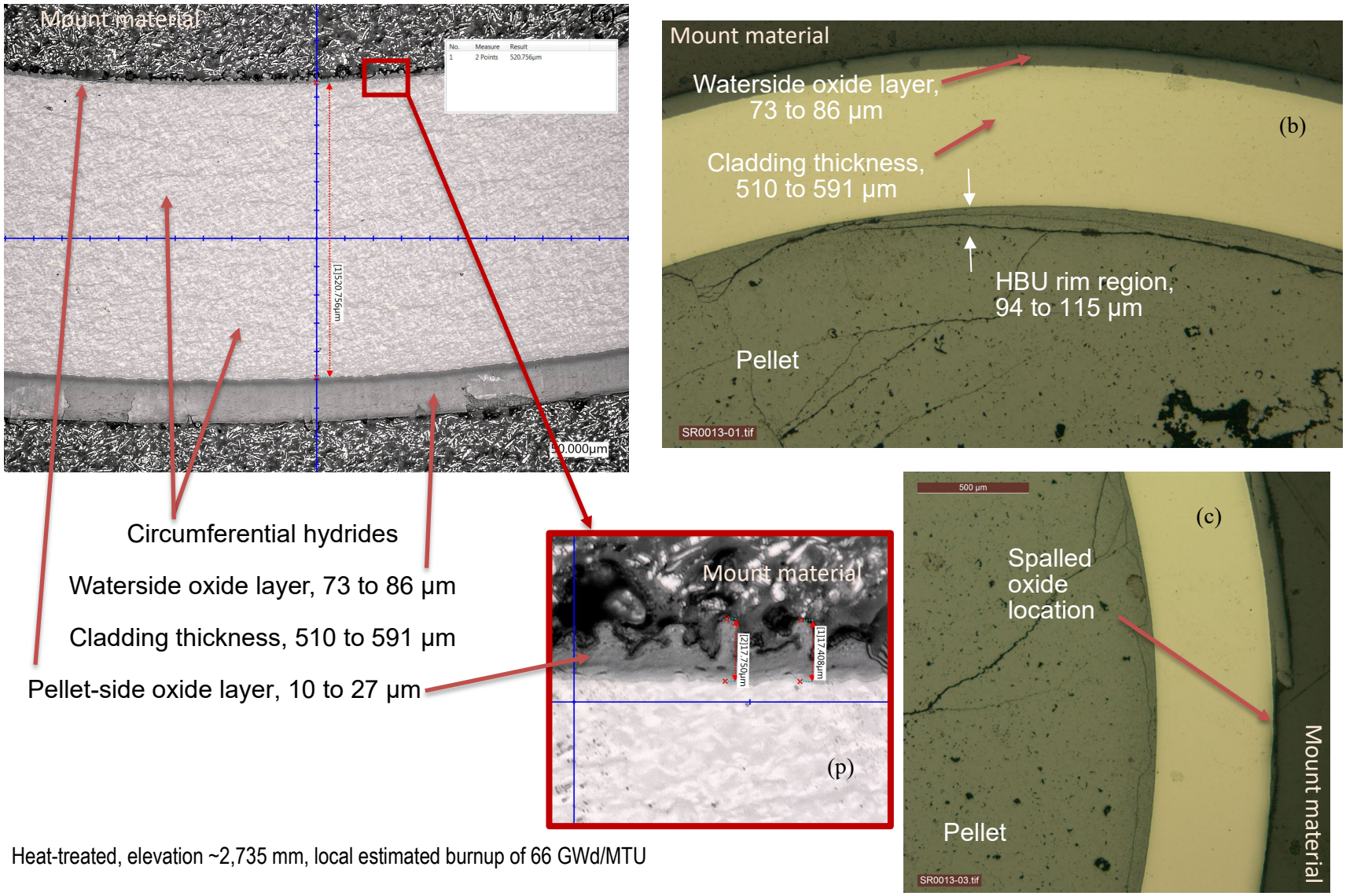

Figure B-24. Selected MET views of heat-treated Zirc-4-clad sister rod F35P17

B-3.4 LT Zirc-4-Clad Sister Rods

Figures B-25 through B-27 provide views of 3A1F05-1260-1279, 3A1F05-2735-2754, and 3A1F05-1585-1604. Views from 3A1F05-1260-1279 and 3A1F05-1585-1604 provided measurement data but were not polished well enough to visualize cladding hydrides. Rod 3A1F05 is a baseline rod that was operated to an average rod burnup of 51 GWd/MTU, as is typical for batch-supplied fuel. The rod is heavily spalled in the higher burnup elevations, including 3A1F05-2735-2754, as shown in the METs. There is a high density of hydrides near the waterside surface of the cladding and a lower density through the remainder of the wall section. Interior hydrides are circumferentially oriented.

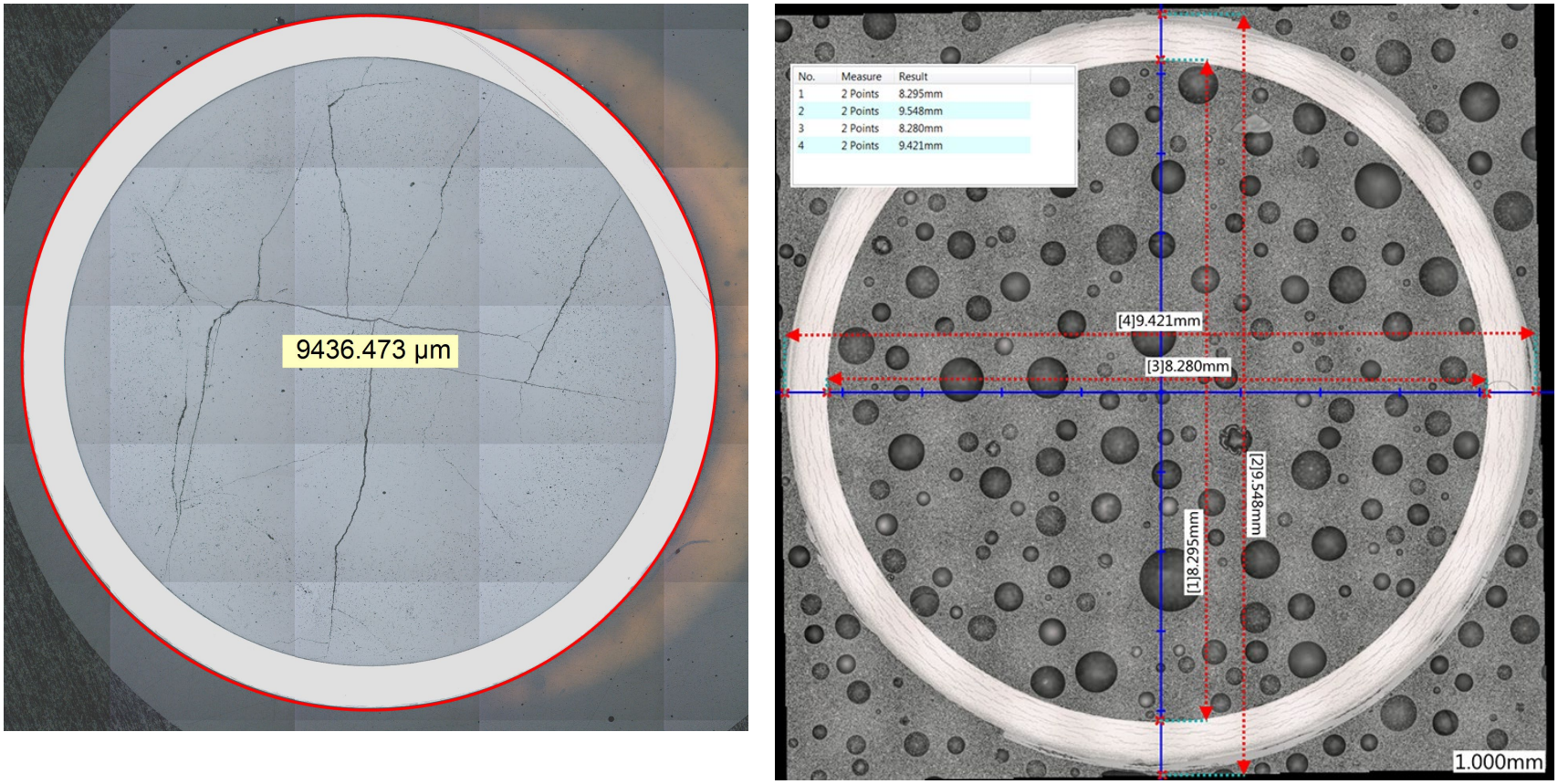

Figure B-25. Fueled overall view of 3A1F05-1260-1279 (left) and 3A1F05-2735-2754 (right) (baseline rod).

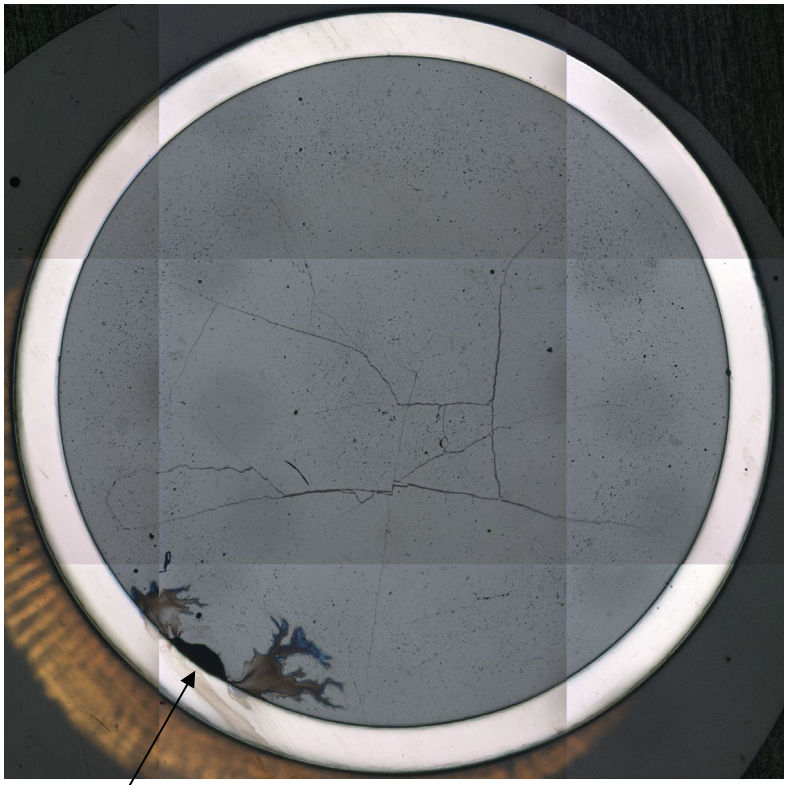

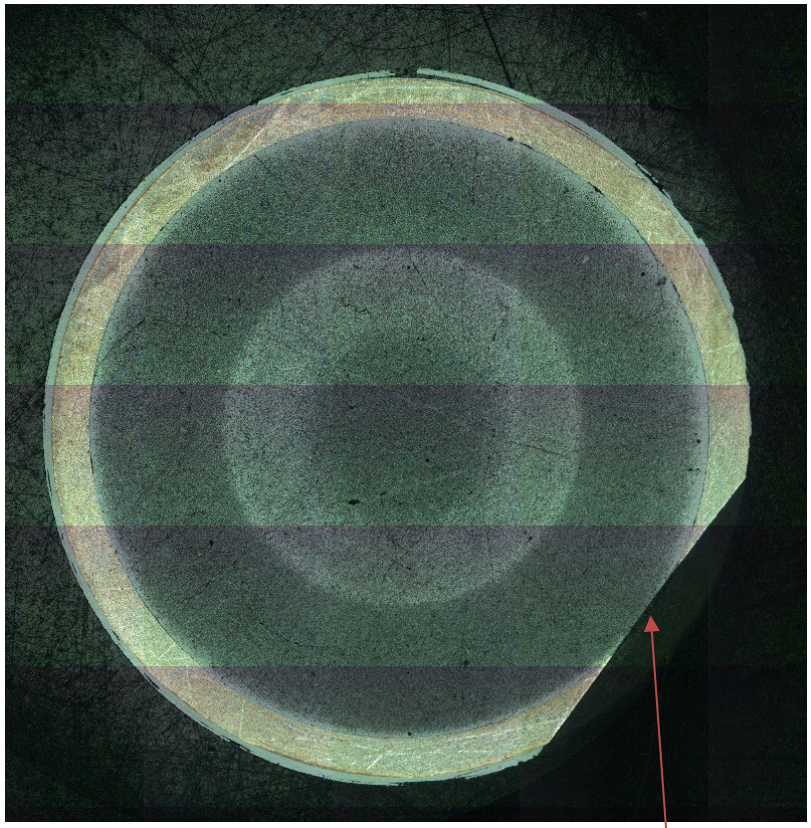

Figure B-26. Fueled overall view of 3A1F05-1585-1604 (left) and 3A1F05-2735-2754 (right) (baseline rod).

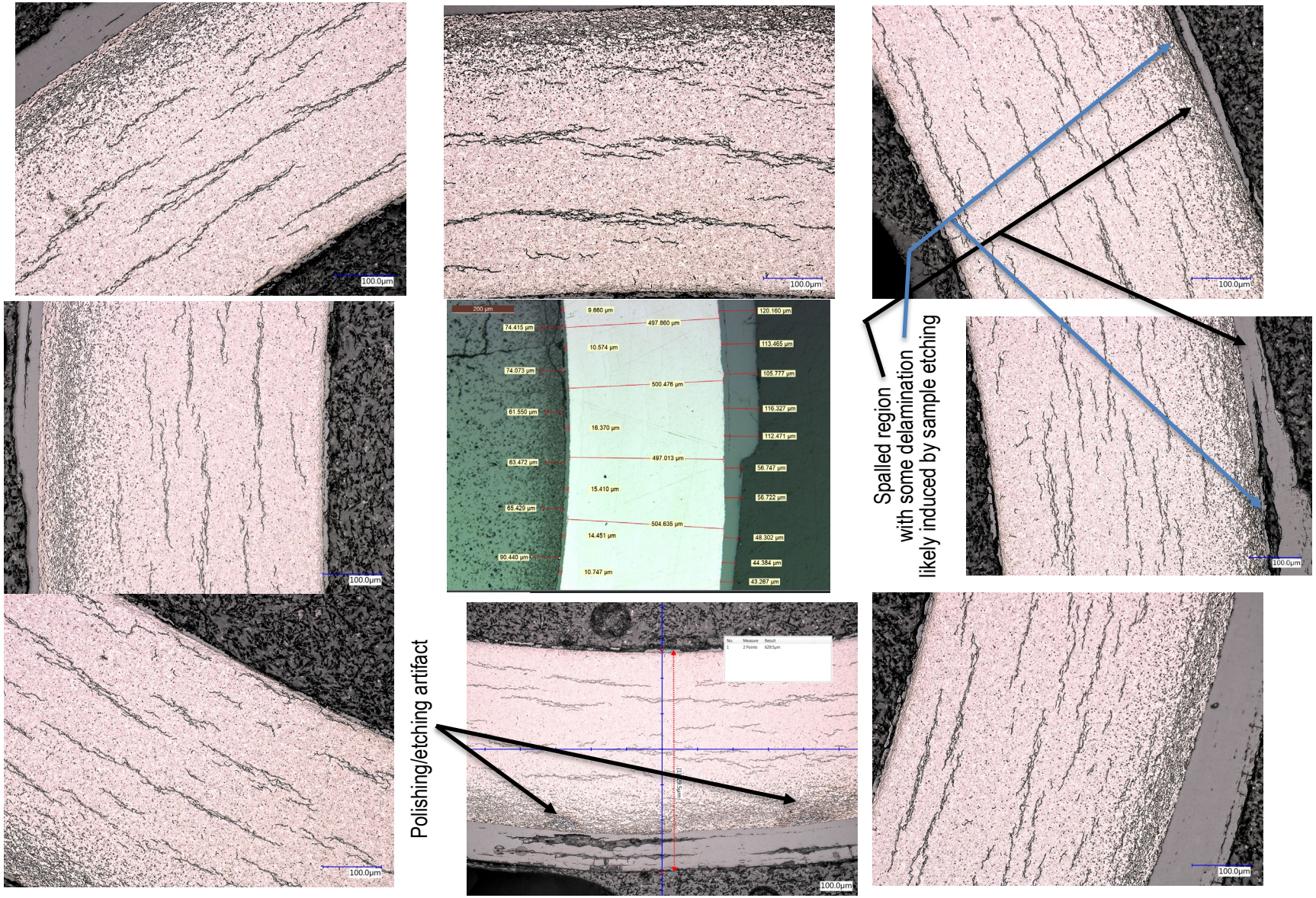

Figure B-27. Magnified views of 3A1F05-2735-2754 (baseline rod).

B-4. CLADDING HYDROGEN MEASUREMENTS (DE.03)

Table B-3 lists the segments that are planned to be used as cladding total hydrogen specimens. To date, 14 of the 20 planned tests have been completed.

B-4.1 Specimen Processing

As shown in Figure B-28, each specimen was cut from the parent segment using a slow speed saw; then each specimen was subsectioned to provide an azimuthal sample for each quadrant (0, 90, 180, and 270°). Although the quadrants are not traceable to the position in the reactor, the azimuthal measurements can provide some indications of variations in cladding hydrogen content resulting from in-reactor temperature differences around the rod's circumference. The oxide layers are not removed from the cladding prior to ONH measurement.

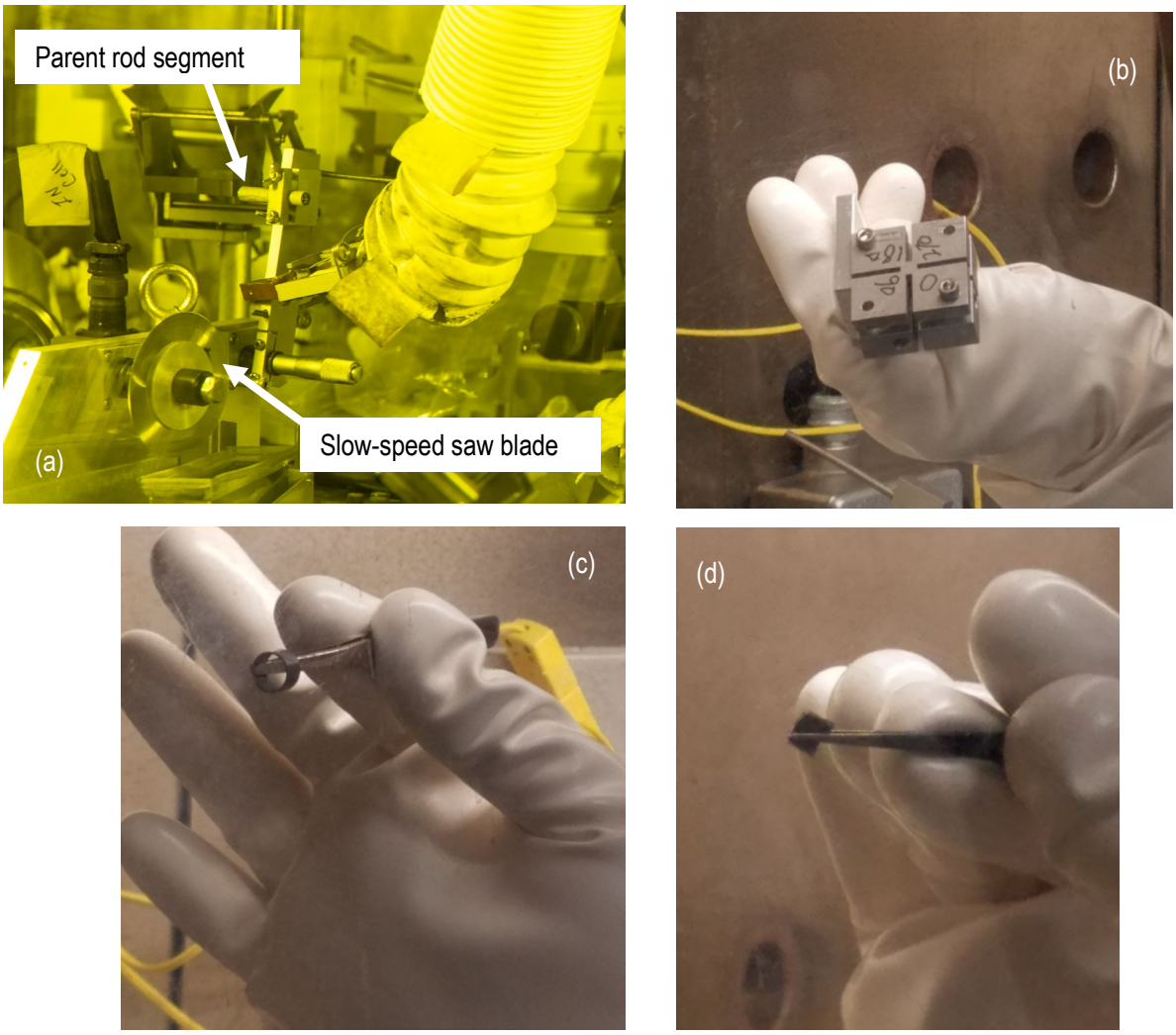

Figure B-28. (a) A parent rod segment mounted in the slow-speed saw in the main hot cell, (b) a bottom view of the fixture used to quarter the 4 mm long defueled cladding specimen, (c) view of the cladding specimen before quartering, and (d) the resulting quadrant sample for LECO ONH measurements.

B-4.2 Analyzer Setup

The LECO Model 836 was placed in a custom enclosure with several glove-ports within the existing IFEL Greenhouse. A second enclosure was place over the LECO transfer port to reduce the potential for contamination during cleaning. Experience with the system showed that the contamination levels were high enough that these enclosures are necessary for adequate contamination control with periodic decontamination of the equipment. The equipment continues to work well with the added enclosures, and no major equipment issues or events have occurred.

The LECO Model 836 ONH analyzer, shown in Figure B-29, uses a destructive method, the *inert gas fusion technique*, to analyze for elemental O, N, and H content. The specimen is melted, thus liberating the O, N, and H, which are captured in a carrier gas and moved through the LECO system for quantification. An ORNL testing protocol was developed based on the manufacturer's recommendations, and helium was chosen as the carrier gas. The standard LECO refractory metals procedure was modified slightly to reduce the generation of carbon contamination from each test. In this method, a LECO 782-720 high-temperature crucible is filled with approximately 0.050 g of graphite powder. The graphite powder is used to ensure good thermal contact between the Ni capsule and the graphite crucible when the capsule drops into the furnace. The instrument is fitted with a LECO 782-721 lower electrode tip that performs the melting. Samples are placed in a LECO 502-344 nickel basket or a LECO 502-822 nickel capsule for analysis, and the remaining metallic slag is disposed of following the test.

The target cladding quadrant sample size is 0.1 g. Instrument tests confirm that variations of specimen mass within the range of the sister rod samples do not influence the results of the tests, as illustrated in Figure B-30. The measurements include hydrogen in the cladding alloy and in the waterside and pelletside oxide layers.

Another consideration for the cladding's hydrogen measurements is the potential influence of room humidity or other sources of hydrogen contamination being introduced into the defueling/cleaning processes. To determine the potential impact, a study was performed that examined the effect of water, ethanol, and acetone exposure on the reported hydrogen in prepared standards. The standards were immersed in the liquid overnight, and then the standards were allowed to air dry. The results, shown in Figure B-31, indicate that a rigorous drying process is not necessary to achieve accurate results for the cladding samples, even at very low hydrogen content.

Before each batch of cladding specimens is tested, the system is calibrated with four standards as having a certified hydrogen content ranging from 9 to 191 ppm. Unfortunately, appropriate calibration standards beyond 191 ppm are not available; therefore, the system cannot be specifically calibrated at the higher hydrogen content expected for the Zirc-4 and LT Zirc-4 cladding and system linearity is assumed.

Typically, industrial users of the machine cite a measurement uncertainty based on the standard deviation of multiple samples from the same specimen, and the quadrant samples for the sister rod specimens are grouped as duplicate samples, with the standard deviation calculated from the four. However, it is known that waterside cladding oxidation and the resulting associated hydrogen content can vary azimuthally; consequently, estimating uncertainty based on the quadrant variation may be overly conservative, and based on the data in hand, the measurement uncertainty is likely ~6.5% (see further discussion in Section B-3.4). Alternatively, the estimated uncertainty can be based on the deviation of the calibration standard measurements from their certified content. The maximum relative error associated with the mass differential study, as shown in Figure B-30, is ±0.5%. The standard deviation associated with the immersion study (shown in Figure B-31) is on the order of ±4 ppm, which is as much a 33% uncertainty at the low hydrogen content (~10 ppm) of the standards used in the study. However, this high level of uncertainty is more likely associated with the lower detection limit of the machine and is not expected to carry through to the higher hydrogen samples. None of these approaches to define the uncertainty are considered particularly accurate. Given the lack of a good basis for assessing uncertainty, the standard

deviation calculated for the 4 azimuthal samples is selected as the most reasonable value pending the acquisition of additional sister rod data.

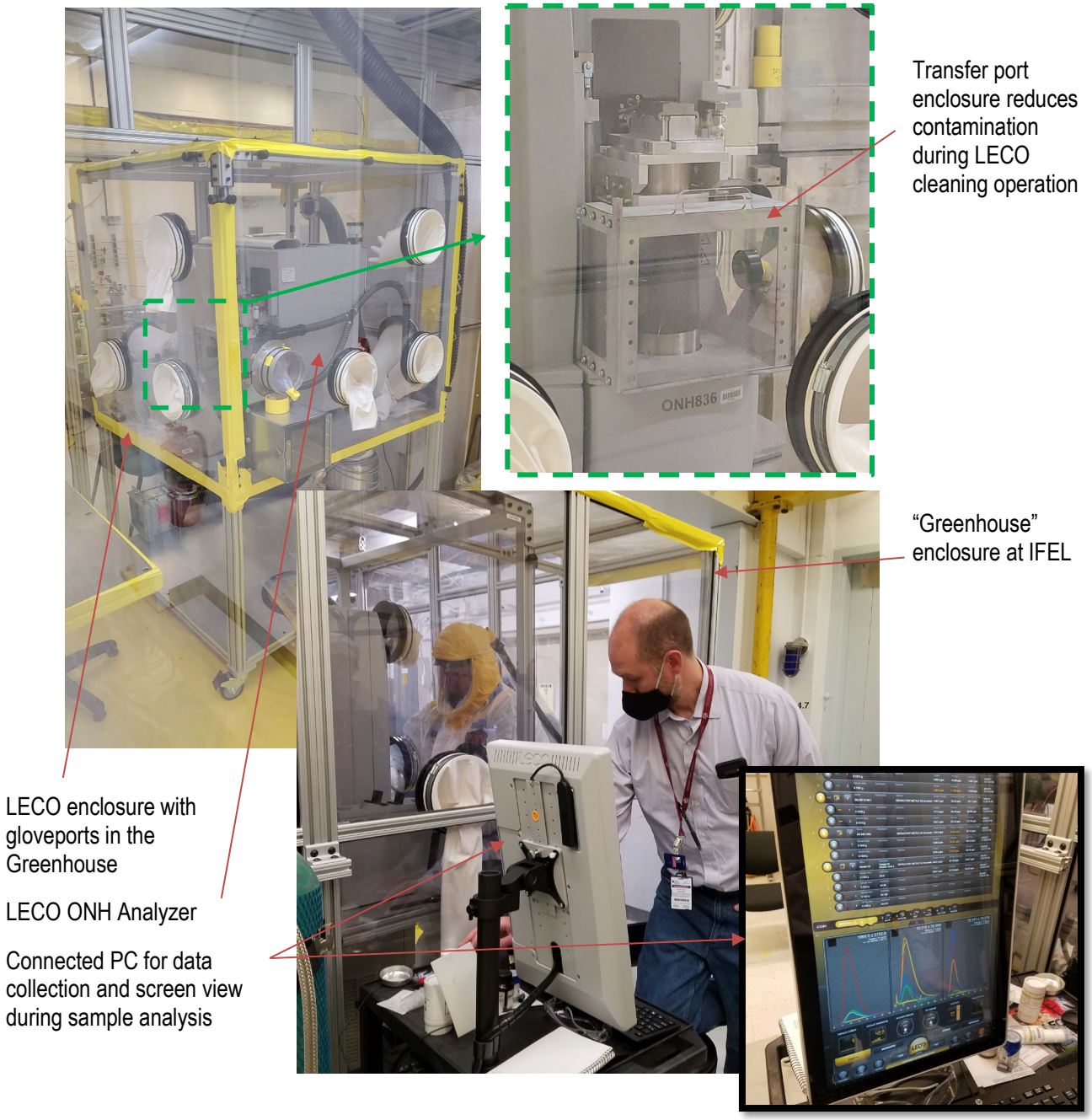

Figure B-29. (a) The LECO ONH Analyzer set up at ORNL's Irradiated Fuels Examination Laboratory with (b) a view of the analysis screen.

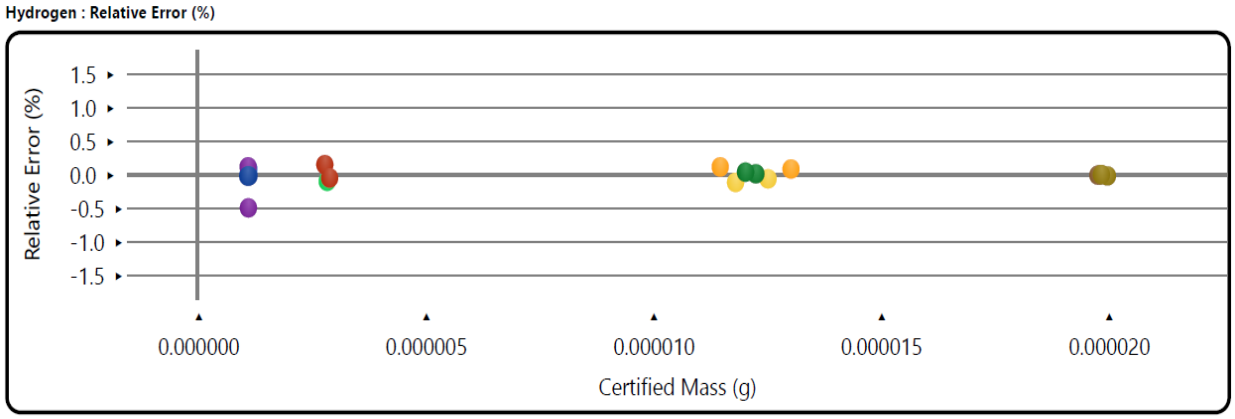

Figure B-30. Reported relative error as a function of standard mass for the calibrated LECO 836 at ORNL, as reported on 5/5/2021.

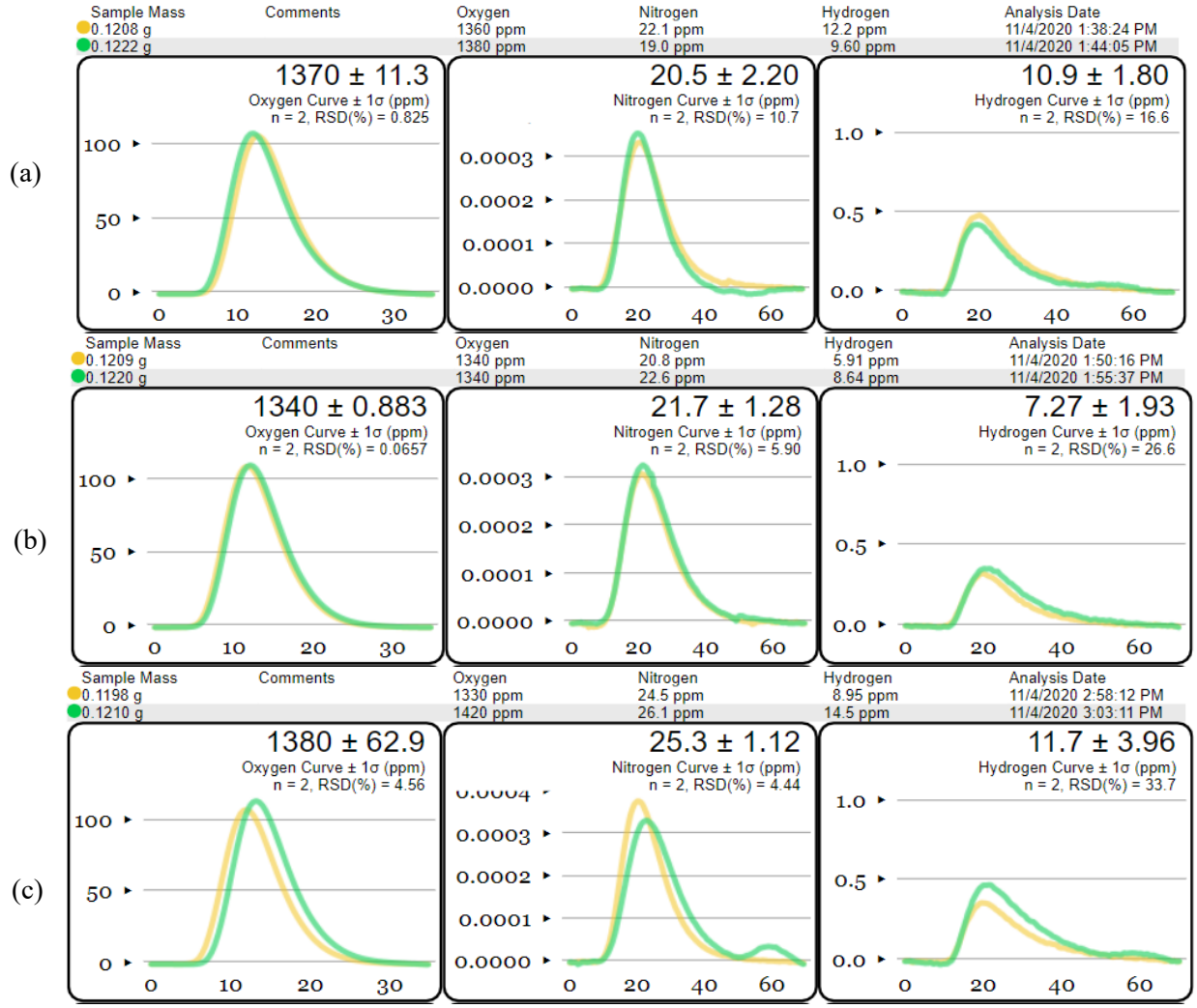

Figure B-31. Results for test standards exposed overnight to (a) water, (b) ethanol, and (c) acetone and then air dried, yielding the same results within uncertainty.

B-4.3 Results

Through August 2021, 14 segments from the phase 1 rods have been analyzed, and the measured hydrogen content is provided in Table B-7. The specimens used for total hydrogen analysis were cut from the parent rod segment into lengths of 4 mm and were defueled in room temperature nitric acid. Each 4 mm specimen was then subsectioned into quarters to provide replicate measurements at each elevation and to provide some information on the azimuthal variation in hydrogen content. Figure B-32 plots the specimen mass vs. the measured hydrogen content for all specimens; no trends were observed with mass. Table B-8 provides the O, N, and H content measured for each specimen and the specimen mass.

Table B-7. Average hydrogen content for samples measured to date.

					Specimen Measured hydrogen content (wppm)			
Parent segment ID	LECO sample name	Cladding Alloy	Estimated local burnup (GWd/MTU)	Mass-weighted average, measured cladding hydrogen, wppm	0° quadrant	90° quadrant	180° quadrant	270° quadrant
30AD05-2410-2429	LH	M5	59	61	59	58	64	63
30AD05-3240-3259	AH	M5	55	141	136	132	146	152
30AE14-1677-1696	PH	M5	60	42	27	45	60	33
30AE14-3399-3418	BH	M5	50	152	152	148	143	166
3A1F05-2006-2025	QH	LT ZIRC 4	56	563	803	377	462	646
3A1F05-2383-2402	NH	LT ZIRC 4	55	684	665	627	469	959
3D8E14-2655-2674	HH	ZIRLO	63	495	363	323	587	708
3D8E14-3206-3225	CH	ZIRLO	59	615	678	654	567	564
3F9N05-1425-1444	MH	ZIRLO	59	130	130	133	128	129
3F9N05-2863-2882	DH	ZIRLO	58	394	394	403	410	371
3F9N05-3331-3350	IH	ZIRLO	51	590	629*		558*	
F35P17-1300-1319	RH	ZIRC 4	65	455	392	301	732	372
F35P17-2735-2754	FH	ZIRC 4	66	872	1,180	879	590	831
F35P17-3050-3069	KH	ZIRC 4	65	1,441	1,350	1,450	1,190	1,770

* The specimen was low in weight and therefore was divided into two quadrants instead of four.

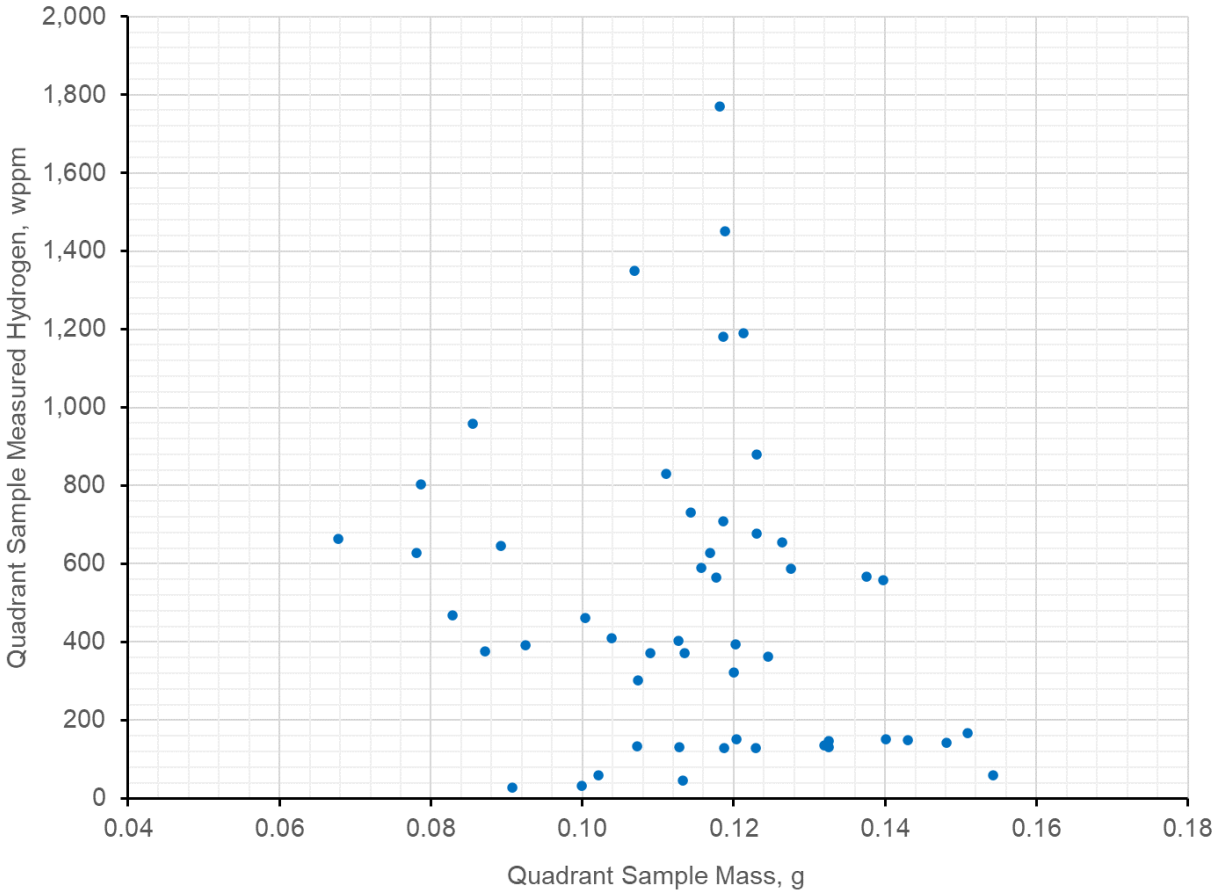

Figure B-32. Measured hydrogen as a function of specimen mass: no trends were observed.

Table B-8. Complete listing of data collected from O, N, and H measurements.

Sample	Mass (g)	O (ppm)	N (ppm)	H (ppm)
AH-0	0.1320	9,230	52	136
AH-90	0.1325	8,980	54	132
AH-180	0.1325	9,080	54	146
AH-270	0.1204	9,340	47	152
BH-0	0.1401	8,590	49	152
BH-90	0.1430	8,330	52	148
BH-180	0.1481	8,290	50	143
BH-270	0.1509	8,510	48	166
CH-0	0.1230	21,900	88	678
CH-90	0.1264	20,700	89	654
CH-180	0.1375	20,400	57	567
CH-270	0.1177	20,300	77	564
DH-0	0.1202	13,400	93	394
DH-90	0.1127	15,100	64	403
DH-180	0.1039	23,600	107	410
DH-270	0.1090	12,800	72	371
FH-0	0.1186	31,300	123	1,180
FH-90	0.1230	32,800	96	879
FH-180	0.1157	32,200	77	590
FH-270	0.1111	31,500	67	831
LH-0	0.1659	7,210	*	58.5
LH-90	0.1543	7,990	*	58.3
LH-180	0.1504	7,880	*	64.0
LH-270	0.1796	7,420	*	63.4

Sample	Mass (g)	O (ppm)	N (ppm)	H (ppm)
HH-0	0.1245	14,600	58	363
HH-90	0.1200	14,500	77	323
HH-180	0.1276	16,600	83	587
HH-270	0.1186	17,600	84	708
IH-0,90*	0.1169	16,300	52	629
IH-180,270*	0.1397	18,000	117	558
KH-0	0.1069	44,500	140	1,350
KH-90	0.1189	41,300	130	1,450
KH-180	0.1213	37,400	119	1,190
KH-270	0.1182	46,100	180	1,770
NH-0	0.0678	24,000	102	665
NH-90	0.0781	25,200	109	627
NH-180	0.0829	23,500	85	469
NH-270	0.0855	23,000	94	959
PH-0	0.0907	6,630	71	27.3
PH-90	0.1133	6,450	34	45.3
PH-180	0.1021	6,620	34	60.6
PH-270	0.0999	6,460	39	33.4
QH-0	0.0787	20,900	118	803
QH-90	0.0871	21,400	106	377
QH-180	0.1004	2,030	50	462
QH-270	0.0893	24,100	92	646
RH-0	0.0925	14,600	**	392
RH-90	0.1073	16,500	**	301
RH-180	0.1143	16,200	**	732
RH-270	0.1135	15,000	**	372
MH-0	0.1128	9,970	**	130
MH-90	0.1072	9,560	**	133
MH-180	0.1187	9,770	**	128
MH-270	0.1229	9,680	**	129

* The specimen was low in weight, so it was divided into two quadrants instead of four.

** The measure scrubber expired, affecting the N measurement for samples containing high O. This issue only impacts the N measurements; it does not impact the O or H measurements.

Figure B-33 plots the average measured cladding hydrogen concentration as a function of the nondestructively measured local average waterside oxide thickness [B-4], and as expected, the two are highly correlated. Based on an analysis of the data in Table B-7, the largest variation in hydrogen content by quadrant was observed for the Zirc-4 and LT Zirc-4 specimens. The best example of azimuthal hydrogen variation is from Sample FH, where the 0° sample had 1,180 ppm H, the 180° sample had 590 ppm H, and the 90 and 270° samples had H contents between these values, at 879 and 831, ppm H respectively. To determine if the variation is related to measurement uncertainty or a true difference in hydrogen content, the measured quadrant oxide thicknesses using eddy current [B-4] for the rod elevations were tabulated (Table B-9), and the mass-weighted average and standard deviations were calculated. The data are plotted in Figure B-34, excluding specimen IH, for which only 2 quadrants were measured. Unfortunately, the information does not conclusively support or refute the theory that the measured circumferential variation of the cladding hydrogen can be ascribed to a true difference in hydrogen content around the cladding circumference as opposed to measurement uncertainty. Further evaluations are planned, and for the time being, the reported 1σ standard deviation is assigned as the uncertainty. One population (the M5 cladding) has a very thin oxide layer, and there is very little azimuthal variation in the hydrogen measurements. Therefore, the azimuthal variation of these rods is likely fully attributable to measurement uncertainty at a magnitude of ~6.5%.

Table B-9. Quadrant cladding hydrogen and quadrant local oxide thickness standard deviation.

Specimen parent segment ID	LECO sample name	Cladding alloy	Mass-weighted average, measured cladding hydrogen, wppm	1σ, cladding hydrogen quadrant, wppm	Average measured local oxide thickness, µm [B-4]	1σ, local oxide thickness quadrant, µm [B-4]
30AD05-2410-2429	LH	M5	61	3	8	1
30AD05-3240-3259	AH	M5	141	9	20	1
30AE14-1677-1696	PH	M5	42	15	8	2
30AE14-3399-3418	BH	M5	152	10	27	2
3A1F05-2006-2025	QH	LT ZIRC 4	563	190	82	10
3A1F05-2383-2402	NH	LT ZIRC 4	684	204	100	7
3D8E14-2655-2674	HH	ZIRLO	495	183	42	8
3D8E14-3206-3225	CH	ZIRLO	615	59	64	9
3F9N05-1425-1444	MH	ZIRLO	130	2	11	4
3F9N05-2863-2882	DH	ZIRLO	394	17	44	9
3F9N05-3331-3350	IH	ZIRLO	590	N/A	62	28
F35P17-1300-1319	RH	ZIRC 4	455	193	43	5
F35P17-2735-2754	FH	ZIRC 4	872	242	91	13
F35P17-3050-3069	KH	ZIRC 4	1,441	245	150	15

Figure B-35 plots the average specimen measured hydrogen content as a function of burnup with available previous measurements. The data are higher previous data; however, the measured hydrogen reported in Table B-9 includes both the metal and the oxide layers. The oxide layer includes hydrogen that was not picked up by the cladding. Figure B-36 plots the measured average cladding hydrogen measurements with the rod axial elevation as measured from the bottom of the rod. The relative

magnitude of the measured hydrogen concentration trends well with the relative magnitude of the oxide thickness.

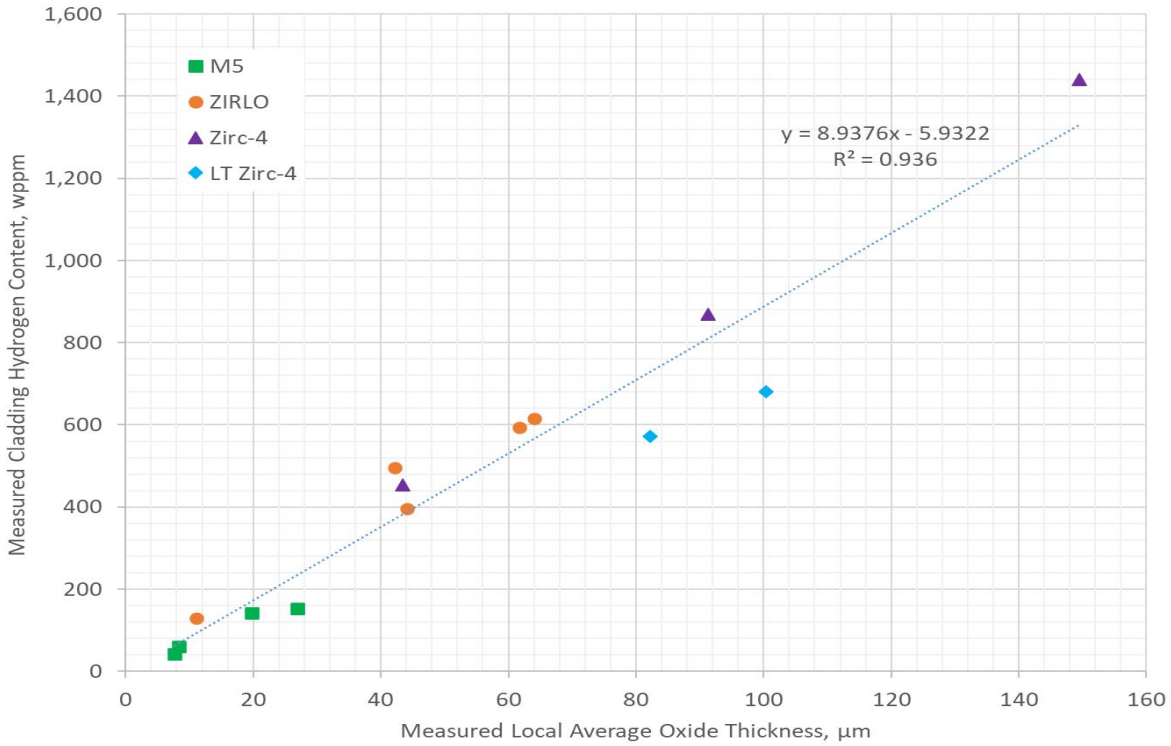

Figure B-33. Mass-weighted average measured cladding hydrogen content as a function of measured average local oxide thickness.

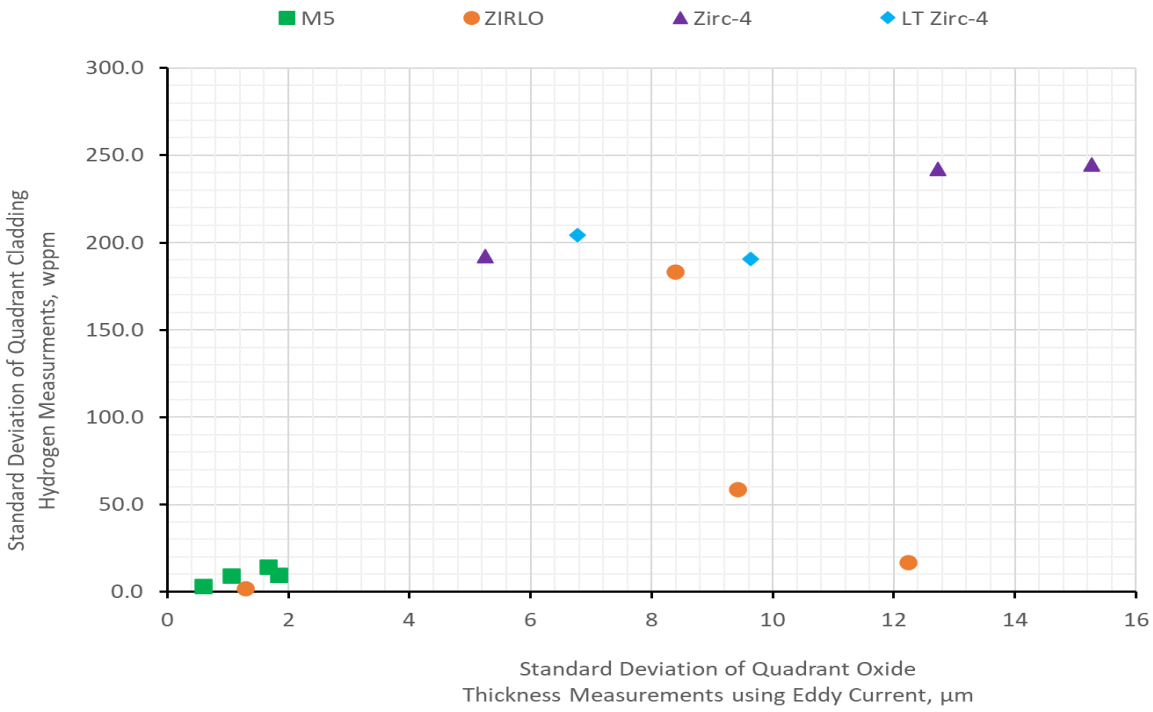

Figure B-34. Standard deviation of quadrant cladding hydrogen measured vs. standard deviation of quadrant oxide thickness from eddy current.

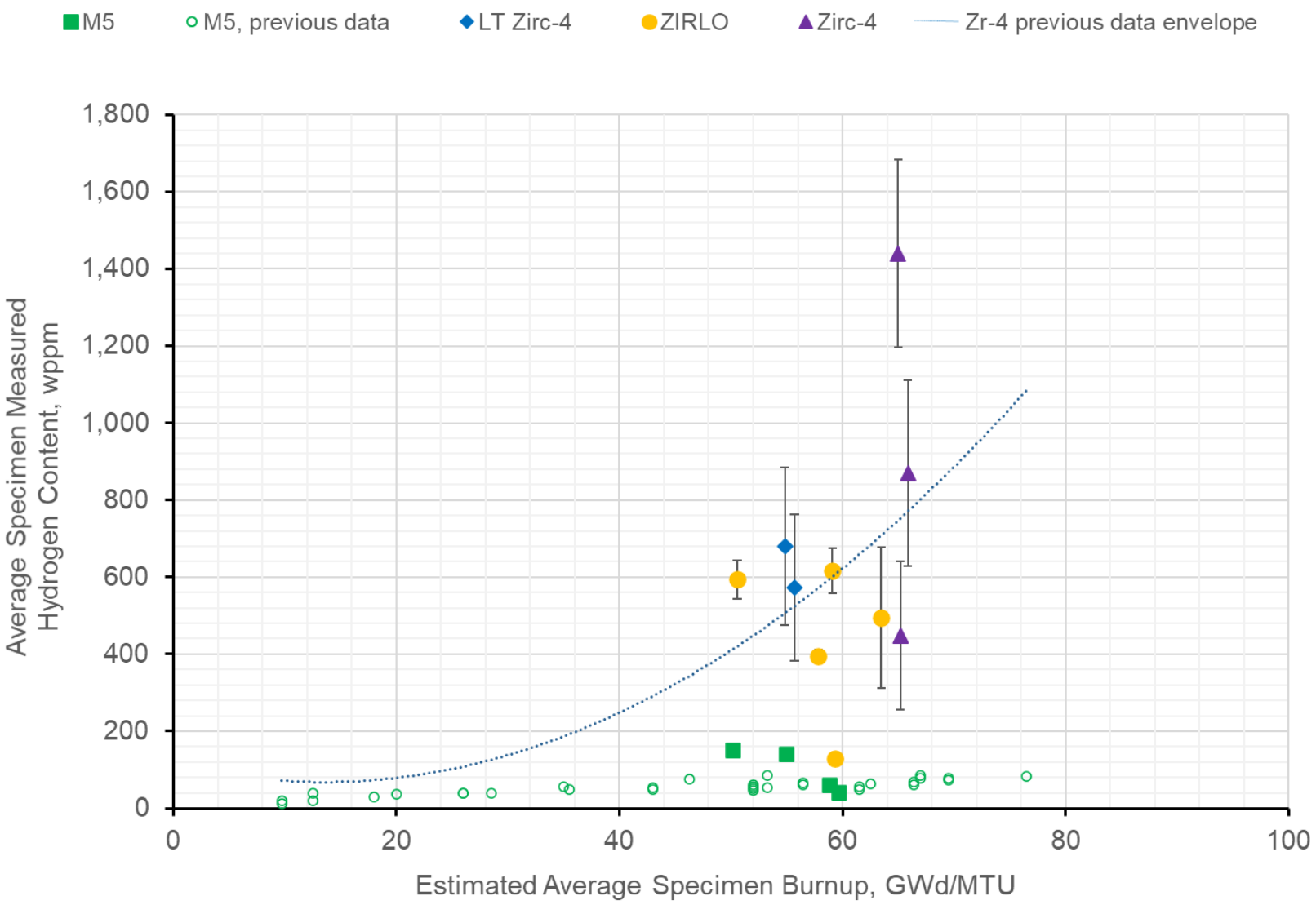

Figure B-35. Average specimen measured hydrogen content as a function of estimated local burnup by alloy and with available previous data.

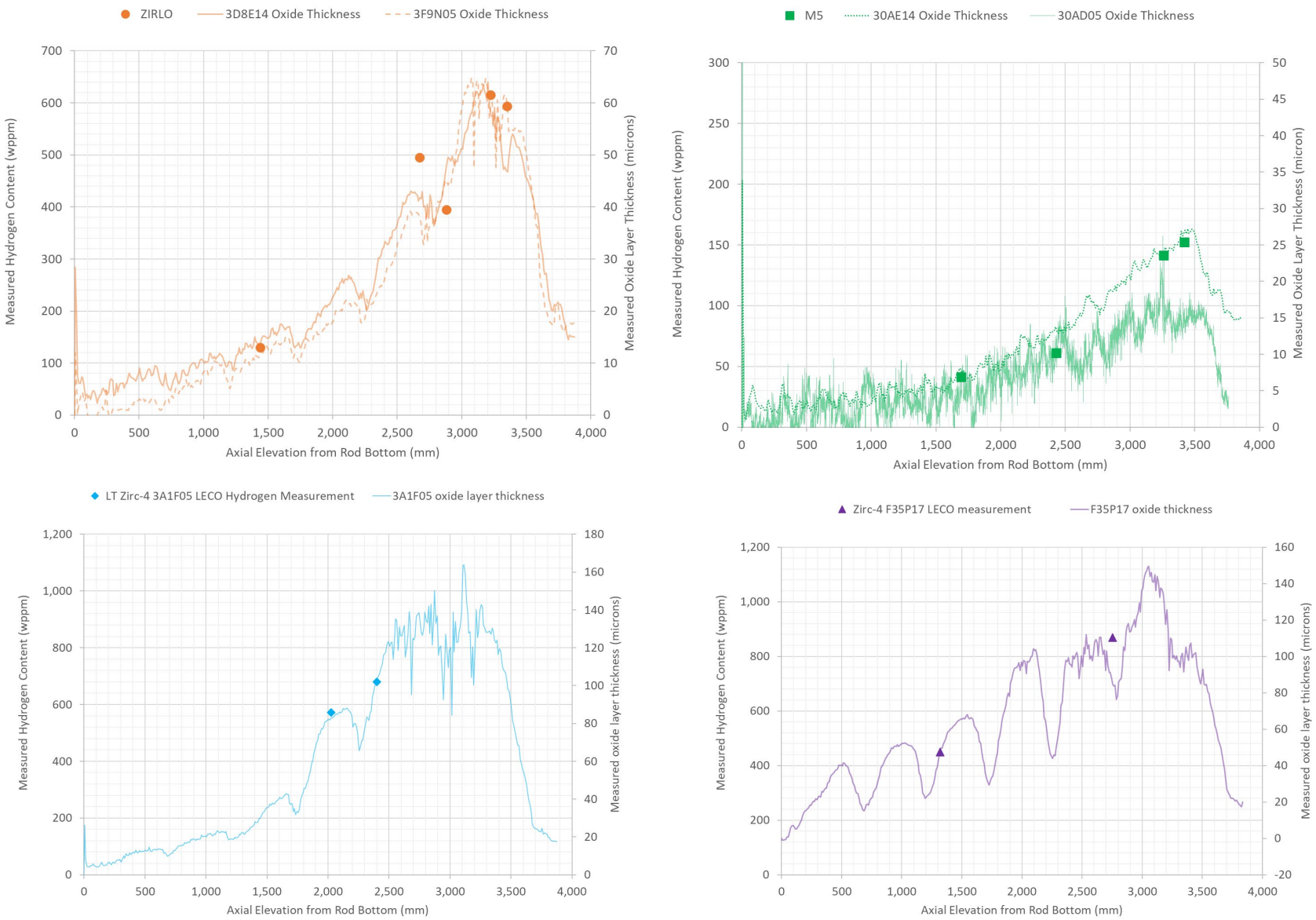

Figure B-36. Measured hydrogen content plotted with rod axial elevation and compared with oxide thickness profile, (a) ZIRLO, (b) M5, (c) LT-Zirc-4, and (d) Zirc-4.

The hydrogen pickup (HPU) is defined as the fraction of the hydrogen generated by the corrosion ($H_{generated}$) that is retained by the cladding ($H_{absorbed}$):

$$HPU = \frac{H_{absorbed}}{H_{generated}} \quad \text{(B-1)}$$

The hydrogen is generated from the waterside oxidation of the zirconium-based cladding alloy with the coolant in reactor:

$$Zr + 2H_2O \Leftrightarrow ZrO_2 + 4H, \quad \text{(B-2)}$$

Thus, for every mole of ZrO_2 created, 4 moles of H are generated. Multiplying the molar ratio by the molar mass, 4 g H/mole H and 123.22 g ZrO_2/mole ZrO_2 = 4 g H/ 123.22 g ZrO_2, the total hydrogen generated is the product of this ratio and the mass of oxide created

$$\frac{4\ g\ H}{123.22\ g\ ZrO_2} t_{ox}\ \rho_{ZrO2} \quad \text{(B-3)}$$

where t_{ox} is the measured thickness of the waterside oxide layer and ρ_{ox} is the density of ZrO_2 (5.6 g/cc).

Given the measured hydrogen concentration in the cladding sample, H in wppm, the mass of hydrogen that was absorbed by the cladding is calculated as

$$H_{absorbed} = H(in\ wppm)\rho_{Zr} t_m\ . \quad \text{(B-4)}$$

where t_m is the remaining cladding wall (metal) thickness and ρ_{Zr} is the density of zirconium (6.5 g/cc). Combining Eq. B-3 and B-4 and applying units of μm for oxide thickness, g/cc for density, and mm for remaining metal thickness, the percentage of HPU is

$$\%HPU = \frac{3.08\ H\ \ \rho_{Zr} t_m}{t_{ox}\ \rho_{ZrO_2}}$$

The calculated HPU is presented in Table B-10. Because metallographic measurements are not yet available for all specimens, several were estimated using the nondestructive measurement data of the oxide thickness and the remaining metal thickness, and typical values were applied for the pellet-side oxide layer thickness. These values will be updated as the MET measurement data become available. The data are consistent with the general performance data available for the alloys and with Pacific Northwest National Laboratory data for the sister rods.

The measurements of the hydrogen concentration reported in Table B-9 and used to calculate %HPU include hydrogen within the waterside oxide layer in addition to the hydrogen in the metal; therefore, the hydrogen pickup of the alloy is overestimated. However, Eq. B-3 assumes that the oxide layer is 100%-dense monoclinic oxide. As the oxide layer grows, its density decreases to about 90%, mainly due to cracking and Eq. B-3 tends to overestimate the amount of oxidation and corresponding available hydrogen, thus underestimating the actual hydrogen pickup. These effects offset each other, and direct measurement of the oxide layer density and hydrogen content are impractical. Although the difference is likely small, in future, the calculation may be repeated using the measured oxygen content (as corrected for oxygen in the as-fabricated cladding) as an additional point for comparison.

The HPU is plotted with oxide thickness in Figure B-37, with the specimen elevation on the rod in Figure B-38, and with estimated local burnup in Figure B-39. A general trend is not evident with oxide thickness or local burnup, but the rod elevation plot (Figure B-38) seems to trend well with %HPU, except for some scatter, and this makes sense because corrosion is a function of time at temperature.

Table B-10. Calculated %HPU Based on Measured Cladding Hydrogen Concentration.

Specimen	HPU (%)	Oxide thickness/remaining wall thickness basis
30AD05-2410-2429	15.0	Nondestructive measurements
30AD05-3240-3259	13.8	Metallography
30AE14-1677-1696	11.3	Nondestructive measurements
30AE14-3399-3418	11.4	Metallography
3A1F05-2006-2025	12.7	Nondestructive measurements
3A1F05-2383-2402	12.1	Nondestructive measurements
3D8E14-2655-2674	23.0	Metallography
3D8E14-3206-3225	19.6	Nondestructive measurements
3F9N05-1425-1444	24.3	Nondestructive measurements
3F9N05-2863-2882	17.9	Nondestructive measurements
3F9N05-3331-3350	19.0	Metallography
F35P17-1300-1319	19.7	Nondestructive measurements
F35P17-2735-2754	17.9	Metallography
F35P17-3050-3069	16.9	Nondestructive measurements

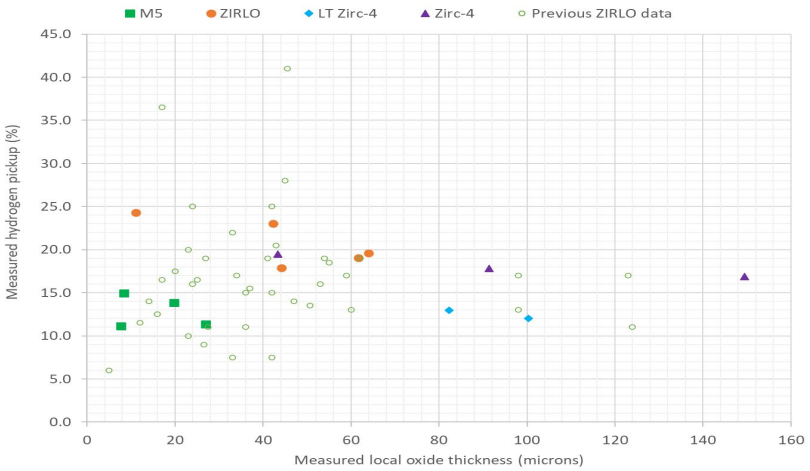

Figure B-37. %HPU as a function of local measured oxide thickness, including publicly available data o ZIRLO [B-7].

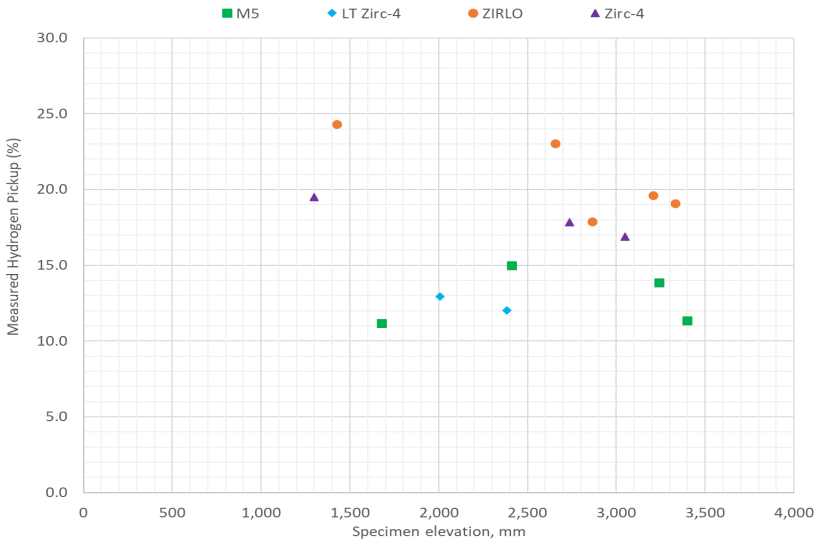

Figure B-38. %HPU as a function of specimen elevation on the fuel rod (multiple rods represented).

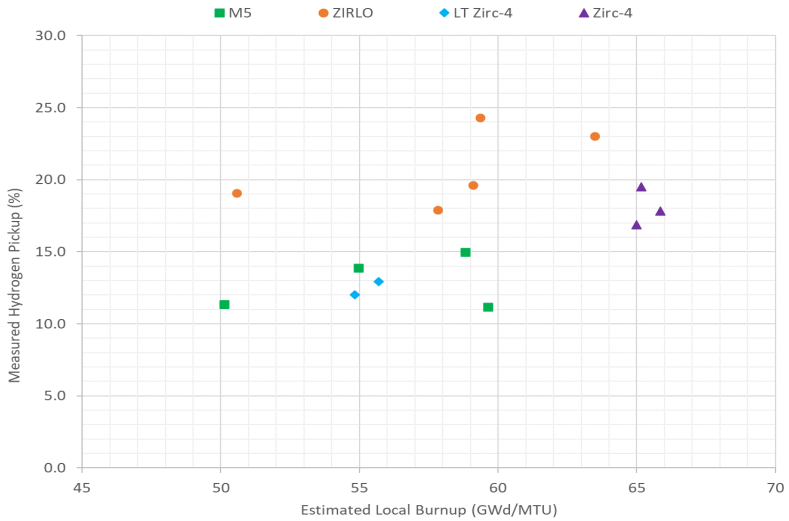

Figure B-39. %HPU as a function of estimated local burnup.

REFERENCES

[B-1.] *High Burnup Dry Storage Cask Research and Development Project: Final Test Plan*, Contract No. DE-NE-0000593, Electric Power Research Institute, Palo Alto, California (2014).

[B-2.] Saltzstein, Sylvia, et al., *Visualization of the High Burnup Spent Fuel Rod Phase 1 Test Plan*, SAND2018-8042-O (2018).

[B-3.] Montgomery, R. A., et al., *Post-Irradiation Examination Plan for High Burnup Demonstration Project Sister Rods*, SFWD-SFWST-2017-000090 ORNL/SR-2016/708, Oak Ridge National Laboratory (2016).

[B-4.] Montgomery, R. A., et al., *Sister Rod Nondestructive Examination Final Report*, SFWD-SFWST-2017-000003 Rev. 1 (M2SF-17OR010201021) / ORNL/SPR-2017/484 Rev. 1 (ORNL/SPR-2018/801), Oak Ridge National Laboratory (2019).

[B-5.] Balfour, M. G., et al. *Corrosion of Zircaloy-Clad Fuel Rods in High-Temperature PWRs: Measurement of Waterside Corrosion in North Anna Unit 1, Interim Report, March 1992*, prepared by Westinghouse Electric Corporation for Electric Power Research Institute, TR-1004008, Tier 2 Research Project 2757-1, 1992.

[B-6.] Cole, S. E. C. Delafoy, R.F. Graebert, P-H. Louf, and N. Teboul. AREVA Optimized Fuel Rods for LWRs, *TopFuel 2012*.

[B-7.] Garde A.M., Slagle W.H., Mitchell D.B., Hydrogen Pick-Up Fraction for ZIRLO™ Cladding Corrosion and Resulting Impact on the Cladding Integrity, Paper 2136, Proceedings of Top Fuel 2009 Paris, France, September 6-10, 2009.